

Delocalized Electrochemical Exfoliation toward High-throughput Fabrication of High-quality Graphene

Penglei Zhang^{1,2}, Peng He^{1,2,*}, Qingkai Yu³, Gang Wang⁴, Tao Huang^{1,2}, Siwei Yang^{1,2}, Xiaosong Liu^{1,2,5}, Zhi Liu^{1,2,5}, Xiaoming Xie^{1,2,5}, Guqiao Ding^{1,2,*}

¹State Key Laboratory of Functional Materials for Informatics, Center for Excellence in Superconducting Electronics, Shanghai Institute of Microsystem and Information Technology, Chinese Academy of Sciences, 865 Changning Road, Shanghai 200050

²College of Materials Science and Opto-Electronic Technology, University of Chinese Academy of Sciences, Beijing 100049, P. R. China

³Ingram School of Engineering and MSEC, Texas State University, San Marcos, Texas 78666, United States

⁴Department of Microelectronic Science and Engineering, Faculty of Science, Ningbo University, Ningbo 315211, P. R. China

⁵School of Physical Science and Technology, ShanghaiTech University, Shanghai 200031, P. R. China

P. Zhang. and P. He. contributed equally.

Abstract

Graphene has well demonstrated its unique properties and advantageous performances in lots of fields during the last 16 years. However, its industrial applications are still impeded by inefficient mass fabrication of high-quality graphene because of the great challenge in deep yet non-destructive graphite exfoliation. Herein, we demonstrated a delocalized electrochemical exfoliation (DEE) technique to efficiently fabricate high-quality graphene. Importantly, chemically transmitting the electric potentials was firstly proposed to spatially extend the exfoliation capability of electric potentials and electrochemically exfoliate every graphite particle dispersed in the electrolyte. The resulting graphene possesses ultralow defect density ($I_D/I_G \sim 0.07$) and extremely high carbon-to-oxygen ratio (~28). Remarkably, high yields (~98.4%, 1-10 layers) and record high production rates (~72.7 g h⁻¹) are realized in up-scaled batch of DEE. Further mechanism investigation revealed that the exfoliation capability of the electric potentials was transmitted to the whole electrolyte system by a dynamically favorable pathway. This pathway includes electrochemical oxidation, intercalation and interlayer bubble generation reactions, which makes deep and non-destructive exfoliation possible for every dispersed graphite particle in a scalable and reproducible manner. This way of using electric potentials differs from existing electrochemical methods and guarantees high throughput as well as high quality. The strategy of delocalized electrochemical exfoliation and the underlying concept of chemically transmitting the electric potentials would accelerate the commercialization of graphene and inspire more efficient fabrication of two-dimensional materials.

Keywords: electrochemical exfoliation, high-quality graphene, scalable production, DFT calculations, strain sensors

1. Introduction

Since the first report of the atomically thin sp^2 carbon layer in 2004¹, graphene has been intensively investigated in the past 16 years and has proven itself a promising candidate in sensors,² energy storage devices³ and composite materials,⁴ etc. However, lacking highly efficient methods to fabricate high-quality graphene lags the coming of ‘graphene era’. To date, only two technological routes for graphene preparation, namely oxidative exfoliation and liquid exfoliation, can be successfully scaled up to several tons per year worldwide.^{5,6} Oxidative exfoliation brings one-atomic-layer graphene oxide (GO) with high yields. Oxidation contributes to deep exfoliation but also creates dense structural defects. These defects cannot be completely removed to restore the electronic properties of graphene even by harsh reduction processes. In contrast, liquid exfoliation of graphite allows direct fabrication of high-quality graphene with simple setups and low costs. However, forces externally applied on edges or surfaces fail to deeply exfoliate graphite flakes; post-screening required to extract the graphene greatly limits the efficiency and scalability. This is reflected by the recent statistical finding from Kauling et al. of 60 commercially available graphene products worldwide, which are fabricated mainly through liquid exfoliation and all of which consist of more than 50% of graphite flakes.⁶ The challenge faced by mass production of high-quality graphene is to simultaneously ensure two desirable but seemly incompatible factors, namely structure integrity and exfoliation efficiency.

A possible solution to balance crystal quality and efficiency is introducing non-destructive intercalation before exfoliation. Specific intercalants bring no/small structural defects and create interlayer gas-generation reactions that drive the exfoliation. However, conventional intercalation procedures such as intercalation of K, Br₂, FeCl₃, Cr₂O₃,⁷⁻¹⁰ generally involve violent and/or toxic processes, which is undesirable for mass production. To the contrary, electrochemical exfoliation is considered as the most potential strategy for high-quality graphene fabrication in large quantities. In this strategy, electric potentials provide green and safe conditions required to induce the intercalation of charged species and generate interlayer bubbles for graphite exfoliation. Utilizing graphite as precursor and electrode(s), the research community have increased the yield and production rate of high-quality graphene to reasonably high levels (~75% and ~32.6 g h⁻¹, respectively).^{11,12} However, the electric potentials induced exfoliation inherently depended on the electric contact between graphite precursor (compressed/bound into the electrodes) and power sources, localizing the electrochemical exfoliation to the electrode(s). Further improving the yield and efficiency is very difficult for existing electrochemical methods. Specifically, bubbles would inevitably fragment the graphite electrode at the same time of exfoliation. Consequently, many graphite particles would uncontrollably detach from the electrode, losing their electric contact before high-degree exfoliation and lowering the graphene yield.¹³ In addition to post-screening, frequent replacement of graphite electrodes or complex device structure is required to scale up the electrochemical exfoliation. Relying on electric potentials that can only trigger graphite exfoliation on the electrode(s), the existing electrochemical methods also cannot well address the quality-efficiency tension. Fabrication of high-quality graphene demands more efficient strategies allowing deep and non-destructive exfoliation of every graphite flake.

Herein, we demonstrate a delocalized electrochemical exfoliation (DEE) method to exfoliate graphite flakes dispersed in the electrolyte into high-quality graphene sheets. By spatially extending the exfoliation capacity of electric potentials, deep and non-destructive exfoliation of graphite was firstly made possible everywhere in the bulk electrolyte. Outstanding structure integrity ($I_D/I_G \sim 0.07$), almost 100% yields (~98.4%, 1-10 layers) and large production rates (~72.7 g h⁻¹ on average in ten batches) were realized in up-scaled fabrication. The DEE-graphene was demonstrated particularly suitable for making high-performance strain sensors with excellent sensitivity and stability. Importantly, a dynamically favorable pathway involving chemical reactions between in-situ electrochemically generated species and graphite was validated to account for the transmission of the electric potentials and the highly efficient electrochemical exfoliation in bulk-phase electrolyte. Chemically transmitting the electric potentials to extend its exfoliation capability not only pave the way for massive production

of high-quality graphene, but also provide new interpretation into electrochemical exfoliation that may inspire more efficient preparation of two-dimensional materials.

2. Results and discussion

Processes of the DEE. The exfoliation was performed in a two-electrode electrochemical system (Figure 1a) powered by a constant current (5 A). Specially, Pt foils were utilized as the electrodes and graphite flakes randomly dispersed in the electrolyte (concentrated sulfuric acid, H_2SO_4) as the graphene precursor. In a typical lab-scale batch (100 mg graphite in 100 mL H_2SO_4), the initial 30-minute electrochemical treatment led to the obvious color change of the graphite flakes from greyish black to blue (Figure 1b). The color change indicated the formation of stage 1 graphite intercalation compounds (GICs),¹⁴ which was further confirmed by the (002) peak shift (from 26.6° for graphite to 22.4° for the blue intermediate) in the X-ray diffraction (XRD)¹⁵ and the disappearance of the 2D band in the Raman spectrum (Figure S1).¹⁶ Following the color change, the volume of the graphite precursor gradually expanded and maximized at around 5 h with an expansion ratio of 65 (Figure S2 and S3), indicating the end of the graphite exfoliation. Thereafter, about 101 mg of purified powder (Figure 1b) was obtained after filtration, repeated rinse with water and complete desiccation. Finally, the powder was added into N,N-dimethylformamide (DMF) and bath-sonicated to prepare the dispersion (1 g L^{-1}) (Figure 1b) used for characterizations. To scale up the electrochemical process, we designed an apparatus with a ring-shaped Pt anode surrounding a Pt cathode (Figure S4a and b). Using this apparatus, 330 g graphite in 6 L H_2SO_4 can be processed into 332.5 g expanded powder and ~332 L (1 g L^{-1}) dispersion (Figure 1c) within about 4.5 h in a typical batch. The average production rate reaches $72.7 \pm 0.4 \text{ g h}^{-1}$ according to the statistical data from 10 batches of up-scaled fabrication.

Characterizations of DEE-graphene. The morphology, thickness and lateral size of the as-prepared product were characterized using atomic force microscopy (AFM), high- resolution transmission electron microscopy (HRTEM), scanning electron microscopy (SEM), high-angle annular dark-field scanning transmission electron microscopy (HAADF-STEM) and scanning tunneling microscopy (STM). HAADF-STEM image (Figure 2a) showed the formation of thin and partially overlapping sheets. Typical data of HRTEM, selected area electron diffraction (SAED) and AFM (Figure 2b, inset and Figure S5) jointly disclosed that two-dimensional and atomically thin sheets compose the product.^{17,18} In most cases of sheet-by-sheet measurement, single- and few-layered sheets were frequently found in the samples (Figure 2b, inset and Figure S6). Further statistical analysis was carried out based on HRTEM images of 127 arbitrarily selected sheets. As presented in Figure 2b, the thickness distribution indicates a yield of ~99.2% (≤ 10 atomic layers) and an average atomic layer count of 2.9. The lateral size of the individual sheet could be precisely determined from its SEM images (Figure 2c, inset and Figure S7). Statistical data of 126 sheets give an average of 5.2 μm in lateral size and a dominant distribution (86.5%) in the range of 1–10 μm (Figure 2c). These results clearly evidence the deep exfoliation of almost every dispersed graphite particles in the electrolyte into micrometer-sized graphene sheets, which can be termed as DEE-graphene.

The structural integrity of the DEE-graphene was probed at the atomic level. In the isolated area (Figure 2d), representative honeycomb lattice of well-organized graphene is observed with a hexagon width of 2.43 \AA and a C-C bond length of 1.44 \AA (Figure 2e) close to the expected value (2.5 \AA and 1.42 \AA) of graphene.¹⁹ Whereas the overlapping area shows obvious Moiré fringes (Figure 2f) that can only appear where two individual graphene layers of high quality densely stack with a proper rotation.²⁰ Also, the typical STM image (Figure 2g and inset) validates the intact crystal structure inherited from the graphite precursor. Raman spectroscopy provides more detailed parameters of the crystal structure. Compared with graphite, the symmetrical 2D band (2700 cm^{-1}) suggested the thinning of graphite sheets to several atomic layers through DEE.²¹ Moreover, uniform D band intensity (1350 cm^{-1}) relative to G band (1580 cm^{-1})²² together with a small average (~ 0.042) confirmed the low content of structure defects (Figure 2h and Figure S8–10). The crystalline domain size (L_a) and defect density (n_p) were determined to be 459.1 nm and $1.3 \times 10^{10} \text{ cm}^{-2}$, which is superior to that of graphene materials fabricated by other exfoliation means and even chemical vapor deposition (CVD) (Figure 2i, Note S1 and Table S1).

Chemical composition was analyzed by X-ray photoelectron spectrometer (XPS) and Fourier transform infrared spectrometer (FT-IR). Approximately 3.3 at. % oxygen (O) is detected, slightly higher than the graphite precursor (2.4 at. %, O). The deconvoluted C 1s spectrum indicates the formation of C-OH (285.6 eV) and C-O-C (286.6 eV) groups (Figure 2j and Figure S11a),²³ instead of functionalities by deep oxidation (such as -COOH, -C=O). This is further confirmed by the characteristic absorption of C-O, C-OH and O-H bonds in the FT-IR spectrum (Figure S11b) of the DEE-graphene.³⁹ Taken together, we can conclude that mild oxidation takes place during the DEE process, but it does not incur excessive structure defects and chemical composition change.

Apart from the lab-scale DEE-graphene discussed above, we also characterized the product prepared through the up-scaled DEE to assess the scalability. Statistic data from HRTEM images indicate an average thickness of 3.2 atomic layers. Among the 61 detected sheets, ~98.4% are not thicker than 10 atomic layers and 88.5% are not thicker than 5 atomic layers. In addition, the yields of graphene in various thickness ranges are inferior to the lab-scale DEE preparation but superior to most reported works (Figure 3a and Figure S12b). For lateral size, micro-sized sheets (~80% in 1–10 μm range) still dominates and the average is almost the same as the lab-scale fabrication. (Figure S12c). Also, Raman and XPS data (Figure S12d–f) revealed chemical composition (3.4 at. % O) and crystal structure ($I_D/I_G\sim 0.07$, $n_D\sim 2.1\times 10^{10} \text{ cm}^{-2}$) similar to that of the DEE-graphene obtained in lab-scale fabrication. The slight decrease of the yield (from 99.2% to 98.4%) and the defect density of the same order of magnitude demonstrates the feasibility of the up-scaled fabrication of high-quality graphene. Importantly, the production rate of the up-scaled DEE increased by 3635 times and reached a record high value (72.7 g h^{-1}) surpassing most reports claiming both outstanding scalability and high quality (Figure 3b, Table S2 and S3). Rationally designed electrodes should be responsible for the successful up-scaling as explained in the following mechanism analysis section. Larger scale preparation is expected by designing more suitable Pt electrodes. Apart from the advantages in scalability, yields, production rates and crystalline quality, it should be noted that DEE shows some other potentials compared with existing methods. Firstly, DEE is independent of any extra hazardous oxidant (i.e., potassium permanganate or perchloric acid) required by many chemical exfoliation methods^{40,41}, which enables DEE to combine the merits of both electrochemical methods (low costs and safe procedures) and chemical exfoliation (outstanding scalability). Secondly, DEE needs no frequent loading and unloading of the graphite electrode as required by existing electrochemical methods to scale up the production. Besides, the electrolyte could be facilely recycled since the whole electrochemical system did not involve any other chemicals except concentrated sulfuric acid (Note S2). The latter two points are expected to greatly lower the production costs. From these characterizations, we can conclude that DEE is a new strategy with clear advantages for the mass production of high-quality graphene.

Mechanism of the DEE. The above characterizations clearly show that DEE enables deep and non-destructive exfoliation of the graphite randomly dispersed in the electrolyte. It is well-established that electric potentials can exfoliate graphite directly contacting with the electrode(s). So, the intermittent electric contact of dispersed graphite flakes with the electrodes may be responsible for the exfoliation at first thought. However, this possibility was ruled out by the control experiments. As presented in Figure S13a–i, the anode, cathode or both electrodes wrapped by Teflon mesh (300 mesh) for physically separating the electrodes and graphite flakes did not prevent the graphite exfoliation. Compared with the existing methods where exfoliation induced by electric potentials can occur only on the electrode(s), these results suggest successful delocalization of electrochemical exfoliation. So, there must be a new mechanism never reported before that delocalizes the electrochemical exfoliation and governs the process of DEE.

To figure it out, we firstly studied the macroscopic phenomena and the corresponding microstructure evolution. During the 5-hour exfoliation, we observed an obvious color change and continuous bubble generation, indicating an exfoliation process composed of intercalation and bubbling exfoliation. Microscopically, the morphology continuously changed from a dense bulk to the exfoliated yet interconnecting network as revealed by the SEM (Figure 4a–h) and optical microscopy (OM) (Figure 4i–p) images. Specially, the OM presents the evolution of the morphology and indicates the role of bubbles as the driving force in the structure evolution. Moreover, the monotonously decreased XRD full

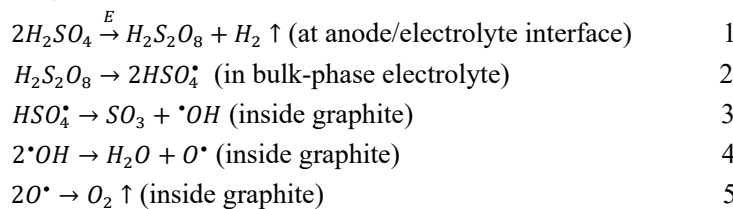
width at half maxima (XRD-FWHM, Figure 4q and Figure S14) and increased MB-based specific surface area (MB-SSA, Figure 4r, Figure S15 and Note S3) jointly and macroscopically confirm the uniform and gradual exfoliation of the dispersed graphite flakes in the electrolyte. A terminal MB-SSA of $829.4 \text{ m}^2 \text{ g}^{-1}$ agrees well with the average atomic layer number (around 2.9) determined by the HRTEM statistics. It should be emphasized that the above characterization results are based on randomly sampled products from the exfoliation system being continuously agitated and homogenized. So, the DEE is a continuous and uniform process that take place in the whole electrolyte system. This is achieved in a system containing only electric potential and the electrolyte that cannot independently exfoliate the graphite. The electric potential across the Pt electrodes undoubtedly plays an important role. We then think it is the spatial extension of the exfoliation capacity of electric potential that results in the delocalized electrochemical exfoliation.

How does the exfoliation capacity of electric potential be spatially extended? We proposed the conception of chemically transmitting the electric potential, trying to explain this new way of electrochemical exfoliation. This transmission was deduced to start by the electrochemical generation of some oxidants since the intercalation and exfoliation processes in DEE partially shares the phenomenon with the oxidant-based bubbling exfoliation.⁴² The formation of the oxidants is proved by the KI-Starch paper (KS) test (Note S4). As seen in Figure 5a, the KS papers turned blue upon the exposure to the electrolyzed H_2SO_4 and became darker blue with the elongated electrolysis time, indicating the generation and accumulation of some oxidative species during H_2SO_4 electrolysis. Furthermore, by respectively collecting the electrolyzed products from the two electrodes for the KS test, we found that the oxidative species was generated selectively near the anode (Figure S16a). These data indicated that the anodic oxidation of H_2SO_4 or/and water (the only two components in the electrolytes) generated certain oxidants. Considering H_2SO_4 being the dominating content (~98%) in the electrolyte, we suppose that $\text{H}_2\text{S}_2\text{O}_8$ originated from H_2SO_4 electrolysis⁴³⁻⁴⁵ (Reaction 1) is the oxidant triggering graphite exfoliation. The formation of $\text{H}_2\text{S}_2\text{O}_8$ is experimentally confirmed by the identification of ambient-stable $\text{Na}_2\text{S}_2\text{O}_8$ in the NaOH-neutralized product of the electrolyzed H_2SO_4 . As shown in Figure 5b, XRD peaks around 19.5° , 26.8° and 27.9° correspond to the characteristic signals of $\text{Na}_2\text{S}_2\text{O}_8$ transformed from the unstable $\text{H}_2\text{S}_2\text{O}_8$ (Note S5).

With the presence of $\text{H}_2\text{S}_2\text{O}_8$, H_2SO_4 molecules intercalate into the graphite layered structure as a result of electronic oxidation and the accordingly reduced friction.⁴⁶ However, how does the exfoliation take place is ambiguous though bubbles are commonly deduced to expand the graphite in other works^{11,42} and are also observed during DEE. More specifically in the case of DEE, bubbles can originate from electrochemical reactions on the surfaces of both electrodes and the decomposition of the unstable $\text{H}_2\text{S}_2\text{O}_8$ into O_2 . But these external bubbles are unlikely to directly exfoliate graphite in a high-efficient manner and are not energetically preferred to enter the graphite interlayers, aggregate and further expand. Therefore, it was unclear how bubbles drive the graphite exfoliation, which is also a long-unsolved problem for persulfate-based graphite exfoliation. For this problem, an unneglectable finding is the participation of graphite in the gas generation. The electrolyzed H_2SO_4 system containing $\text{H}_2\text{S}_2\text{O}_8$ does not release visible bubbles at room temperature. However, the bubbles appear and become abundant upon the introduction of graphite as a result of the gas releasing primarily at the GIC/electrolyzed H_2SO_4 interface (Figure 5c, inset and Figure S17). The gas was proved to be O_2 (Figure S18) and the mean gas generation rate reached as high as 6.5 mL min^{-1} when 100 mg of graphite flakes were introduced into 100 mL 5-hour electrolyzed H_2SO_4 (Figure 5c, Figure S16b-d and Note S6). Based on the above facts, we propose a pathway from $\text{H}_2\text{S}_2\text{O}_8$ formation to the interlayer O_2 generation in DEE. As schematically illustrated in Figure 5d, four steps are involved: (1) Continuous anodic oxidation of HSO_4^- (the dominating specie in H_2SO_4) to accumulate $\text{H}_2\text{S}_2\text{O}_8$ in the bulk liquid; (2) $\text{H}_2\text{S}_2\text{O}_8$ -derived HSO_4^\cdot extracting electrons from graphite and inducing electronic oxidation of graphite to facilitate the intercalation of HSO_4^- into graphite; (3) Electronically oxidized graphite extracting electrons from the intercalated HSO_4^- to form HSO_4^\cdot inside the graphite layers; (4) HSO_4^\cdot radicals disproportionating to form O_2 bubbles and drive the graphite exfoliation.

In this pathway, HSO_4^\cdot radicals forming in the bulk-phase of the electrolyte (out of layers), inside the graphite layers and their interlayer disproportionation were three key steps. Density functional theory

(DFT) calculations validated this pathway as a dynamically favorable one by revealing the energy evolution and the barriers of the involved reactions. As presented in Figure 5e, the overall pathway is an exothermic reaction with an energy decrease of 12.91 eV and the rate-limiting step is the HSO_4^\cdot disproportionation. A small energy barrier (0.78 eV, Table S4) of homolytic $\text{H}_2\text{S}_2\text{O}_8$ cleavage together with the electron spin resonance (ESR, Figure S19) and the liquid chromatography-mass spectra (LC-MS, Figure S20 and Note S7) of the electrolyzed H_2SO_4 jointly confirm the easy formation of HSO_4^\cdot in the bulk electrolyte (Reaction 2). For the rate-limiting step, the energy barrier of HSO_4^\cdot disproportionation (Reaction 3-5) in the galleried (0.91 eV) is much smaller than that in bulk electrolyte (1.76 eV, Table S5 and Figure S21). This indicates the interlayer O_2 generation was more dynamically favorable and also explains our experimental observation that the generation of bubble was slow in the electrolyzed H_2SO_4 but significantly accelerated upon the graphite introduction. Also, the simulation reveals that the increased chemical potential of HSO_4^\cdot inside graphite layers is responsible for the decreased energy barrier of the interlayer disproportionation reactions. Therefore, besides bridging electron transfer, graphite also served as a catalyst for bubble generation (Reaction 3-5) through a spatial confinement effect (Figure S22).



The pathway we made clear above well explain the delocalized exfoliation of graphite initiated by electric potential. On the other hand, the chemical reactions involved in this pathway are essentially driven by electrical potential: $\text{H}_2\text{S}_2\text{O}_8$ and HSO_4^\cdot radicals transfer the electric potential to the chemical potential required by exfoliation. So, it is the chemical pathway that transmits the electric potential to the whole electrolyte system from the perspective of substance change and electron transfer. After the transmission of electric potential, electrochemical exfoliation gets rid of the reliance on the direct graphite/electrode contact that restricts the existing electrochemical methods and makes the deep exfoliation possible for every single graphite particle dispersed in the electrolyte. And only in this way can the electrochemical exfoliation be delocalized and up-scaled by simply enlarging the active area of the Pt anode. So, chemically transmitting electric potentials endows the DEE with merits of both conventional electrochemical methods and the oxidant-based techniques to produce high-quality graphene with ultra-high efficiency and outstanding scalability. In addition, the bubbling exfoliation mechanism revealed here can be expanded to explain the oxidant-based exfoliation using different persulfates as exfoliation agents^{13,42,47}. More importantly, chemically transmitting the electric potential is expected to inspire preparation of other two-dimensional materials in specific exfoliation systems and in an efficient manner.

Properties of the DEE-graphene based strain sensors. Benefiting from the high crystalline quality, excellent conductivity ($1.9 \times 10^5 \text{ S m}^{-1}$ on average) was detected in the layer-structured films assembled from the DEE-graphene (Figure S23a–c and Note S8). Generally, highly conductive graphene sheets are considered good candidates for high-performance strain sensors. To assess the potential of DEE-graphene as sensor material, we constructed conducting networks of DEE-graphene on the flexible substrate (Figure S24a). The resulting sensor shows significant variations in relative resistance upon stretching at small strains (0–7%, Figure 6a). Its sensitivity as reflected by gauge factors (GFs) (Figure 6b) outperform most previously reported^{48–57} counterparts in the same strain range (Table S6). The variations in relative resistance upon stretching to maximum strains of 1%, 3%, 5%, and 7% were measured to be 0.46, 2.13, 5.94, and 75.12, respectively (Figure 6c), and these results are in good agreement with those shown in Figure 6a, which indicates the excellent reliability of the sensor. The almost reversible stretching and releasing behavior (Figure S24b) further validates the repeatability of the sensor. Benefiting from the high sensitivity, the strain sensor can be implemented to detect extremely tiny strains of down to 0.05% (Figure 6d). The response of the sensor to quasi-transient step strain and to 6% strain at different frequencies (0.05–0.8 Hz) reveals a response time less than 100 ms, a recovery

time about 500 ms (Figure 6e) and almost no frequency dependence (Figure 6f), which is the manifestation of excellent stability and rapid response rate. Further, the excellent cycling stability and repeatability at 6% strain as presented in Figure 6g indicate good applicability of the sensor in practical scenario. These properties allow the sensor to easily differentiate finger bending states with different bending angles (30°, 45° and 90°) (Figure S24c).

3. Conclusion

In summary, by chemically transmitting the electric potential, we firstly extend the exfoliation capability of electric potentials to the whole electrolyte system and achieve delocalization of the electrochemical exfoliation. The delocalized electrochemical exfoliation (DEE) made deep and non-destructive exfoliation possible for every graphite particle dispersed in the bulk-phase electrolyte. DEE-graphene with ultralow defect density ($I_D/I_G \sim 0.07$) and extremely high carbon-to-oxygen ratio (~ 28) has been fabricated with an almost 100% yields ($\sim 98.4\%$, 1-10 layers) and record-breaking production rates ($\sim 72.7 \text{ g h}^{-1}$ on average in ten batches) under optimized conditions. This new way of using electrodes solves the quality-efficiency tension confronted by conventional methods. Also, the fabrication costs will be greatly lowered and safety be increased especially in bulk production because of the free of additional oxidant and the recyclable electrolyte (H_2SO_4). Importantly, a dynamically favorable pathway involving chemical reactions between in-situ electrochemically generated species and graphite was validated to account for the transmission of the electric potentials and the highly efficient electrochemical exfoliation in bulk-phase electrolyte. In addition, the revealed mechanism for interlayer bubble generation in the confined space provides new interpretation into the bubble exfoliation of graphite. The obtained high-quality DEE-graphene exhibited potential in fabricating highly sensitive and durable strain sensors. More importantly, the delocalized electrochemical strategy and the underlying concept of chemically extending the electric potential are expected to speed up the coming of the ‘graphene era’ and accelerate the scalable applications of other two-dimensional materials.

ACKNOWLEDGEMENTS

This work was supported by the National Natural Science Foundation of China (Grants 51802337, 11774368, 11804353, 11704204, 11227902 and U1632269) and 'Strategic Priority Research Program (B)' of the Chinese Academy of Sciences (Grants XDB04010600).

References

(1) Novoselov, K. S.; Geim, A. K.; Morozov, S. V; Jiang, D.; Zhang, Y.; Dubonos, S. V.; Grigorieva, I. V; Firsov, A. A. Electric Field Effect in Atomically Thin Carbon Films Supplementary. *Science*. **2004**, *5* (1), 1–12.

(2) Trung, T. Q.; Lee, N. E. Flexible and Stretchable Physical Sensor Integrated Platforms for Wearable Human-Activity Monitoring and Personal Healthcare. *Adv. Mater.* **2016**, *28* (22), 4338–4372.

(3) Lung-Hao Hu, B.; Wu, F. Y.; Lin, C. Te; Khlobystov, A. N.; Li, L. J. Graphene-Modified LiFePO₄ Cathode for Lithium Ion Battery beyond Theoretical Capacity. *Nat. Commun.* **2013**, *4*, 1–7.

(4) Wang, S.; Li, R.; Müllen, K.; Hinkel, F.; Feng, X.; Hernandez, Y.; Puniredd, S. R.; Parvez, K. Electrochemically Exfoliated Graphene as Solution-Processable, Highly Conductive Electrodes for Organic Electronics. *ACS Nano*. **2013**, *7* (4).

(5) Y. Zhu.; H. Ji.; H. Cheng.; R. S. Ruoff. Mass Production and Industrial Applications of Graphene Materials. *Nat. Sci. Rev.* **2018**, *5*, 90–101.

(6) Kauling, A. P.; Seefeldt, A. T.; Pisoni, D. P.; Pradeep, R. C.; Bentini, R.; Oliveira, R. V. B.; Novoselov, K. S.; Castro Neto, A. H. The Worldwide Graphene Flake Production. *Adv. Mater.* **2018**, *30* (44), 1–6.

(7) Viculis, L. M.; Mack, J. J.; Mayer, O. M.; Hahn, H. T.; Kaner, R. B. Intercalation and Exfoliation Routes to Graphite Nanoplatelets. *J. Mater. Chem.* **2005**, *15* (9), 974–978.

(8) Bardhan, K. K.; Chung, D. D. L. A Kinetic Model of the First Intercalation of Graphite. *Carbon* **1980**, *18* (5), 303–311.

(9) Zhao, W.; Tan, P. H.; Liu, J.; Ferrari, A. C. Intercalation of Few-Layer Graphite Flakes with FeCl₃: Raman Determination of Fermi Level, Layer by Layer Decoupling, and Stability. *J. Am. Chem. Soc.* **2011**, *133* (15), 5941–5946.

(10) Wang, F.; Li, W.; Hou, M.; Li, C.; Wang, Y.; Xia, Y. Sandwich-like Cr₂O₃-Graphite Intercalation Composites as High-Stability Anode Materials for Lithium-Ion Batteries. *J. Mater. Chem. A* **2015**, *3* (4), 1703–1708.

(11) Parvez, K.; Wu, Z. S.; Li, R.; Liu, X.; Graf, R.; Feng, X.; Müllen, K. Exfoliation of Graphite into Graphene in Aqueous Solutions of Inorganic Salts. *J. Am. Chem. Soc.* **2014**, *136* (16), 6083–6091.

(12) Yang, S.; Ricciardulli, A. G.; Liu, S.; Dong, R.; Lohe, M. R.; Becker, A.; Squillaci, M. A.; Samori, P.; Müllen, K.; Feng, X. Ultrafast Delamination of Graphite into High-Quality Graphene Using Alternating Currents. *Angew. Chemie - Int. Ed.* **2017**, *56* (23), 6669–6675.

(13) Dimiev, A. M.; Ceriotti, G.; Metzger, A.; Kim, N. D.; Tour, J. M. Chemical Mass Production of Graphene Nanoplatelets in ~100% Yield. *ACS Nano*. **2016**, *10* (1), 274–279.

(14) Dimiev, A. M.; Bachilo, S. M.; Saito, R.; Tour, J. M. Reversible Formation of Ammonium Persulfate/Sulfuric Acid Graphite Intercalation Compounds and Their Peculiar Raman Spectra. *ACS Nano*. **2012**, *6* (9), 7842–7849.

(15) Saito, R.; Dimiev, A. M.; Tour, J. M.; Pasquali, M.; Behabtu, N.; Ceriotti, G.; Zakhidov, D. Direct Real-Time Monitoring of Stage Transitions in Graphite Intercalation Compounds. *ACS Nano*. **2013**, *7* (3), 2773–2780.

(16) Pei, S.; Wei, Q.; Huang, K.; Cheng, H. M.; Ren, W. Green Synthesis of Graphene Oxide by Seconds Timescale Water Electrolytic Oxidation. *Nat. Commun.* **2018**, *9* (1), 1–9.

(17) Cheng, Z.; Zhou, Q.; Wang, C.; Li, Q.; Wang, C.; Fang, Y. Toward Intrinsic Graphene Surfaces: A Systematic Study on Thermal Annealing and Wet-Chemical Treatment of SiO₂-Supported Graphene Devices. *Nano Lett.* **2011**, *11* (2), 767–771.

(18) Hernandez, Y.; Nicolosi, V.; Lotya, M.; Blighe, F. M.; Sun, Z.; De, S.; McGovern, I. T.; Holland, B.; Byrne, M.; Gun'ko, Y. K.; et al. High-Yield Production of Graphene by Liquid-Phase Exfoliation of Graphite. *Nat. Nanotechnol.* **2008**, *3* (9), 563–568.

(19) Hernandez, Y.; Coleman, J. N.; Wang, Z.; King, P. J.; Duesberg, G. S.; Nicolosi, V.; Blighe, F. M.; De, S.; McGovern, I. T.; Karlsson, L. S.; et al. Liquid Phase Production of Graphene by Exfoliation of Graphite in Surfactant/Water Solutions. *J. Am. Chem. Soc.* **2009**, *131* (10), 3611–3620.

(20) Warner, J. H.; Rümmeli, M. H.; Gemming, T.; Büchner, B.; Briggs, G. A. D. Direct Imaging of Rotational Stacking Faults in Few Layer Graphene. *Nano Lett.* **2009**, *9* (1), 102–106.

(21) Lu, J.; Yang, J. X.; Wang, J.; Lim, A.; Wang, S.; Loh, K. P. One-Pot Synthesis of Fluorescent Carbon Nanoribbons, Nanoparticles, and Graphene by the Exfoliation of Graphite in Ionic Liquids. *ACS Nano*. **2009**, *3* (8), 2367–2375.

(22) Ferrari, A. C.; Meyer, J. C.; Scardaci, V.; Casiraghi, C.; Lazzeri, M.; Mauri, F.; Piscanec, S.; Jiang, D.; Novoselov, K. S.; Roth, S.; et al. Raman Spectrum of Graphene and Graphene Layers. *Phys. Rev. Lett.* **2006**, *97* (18), 1–4.

(23) Huang, H.; Xia, Y.; Tao, X.; Du, J.; Fang, J.; Gan, Y.; Zhang, W. Highly Efficient Electrolytic Exfoliation of Graphite into Graphene Sheets Based on Li Ions Intercalation-Expansion-Microexplosion Mechanism. *J. Mater. Chem.* **2012**, *22* (21).

(24) Green, A. A.; Hersam, M. C. Solution Phase Production of Graphene with Controlled Thickness via Density Differentiation. *Nano Lett.* **2009**, *9* (12), 4031–4036.

(25) Lin, T.; Chen, J.; Bi, H.; Wan, D.; Huang, F.; Xie, X.; Jiang, M. Facile and Economical Exfoliation of Graphite for Mass Production of High-Quality Graphene Sheets. *J. Mater. Chem. A* **2013**, *1* (3), 500–504.

(26) Knieke, C.; Berger, A.; Voigt, M.; Klupp Taylor, R. N.; Röhrl, J.; Peukert, W. Scalable Production of Graphene Sheets by Mechanical Delamination. *Carbon*. **2010**, *48* (11), 3196–3204.

(27) Arao, Y.; Mizuno, Y.; Araki, K.; Kubouchi, M. Mass Production of High-Aspect-Ratio Few-Layer-Graphene by High-Speed Laminar Flow. *Carbon*. **2016**, *102*, 330–338.

(28) Paton, K. R.; Varrla, E.; Backes, C.; Smith, R. J.; Khan, U.; O'Neill, A.; Boland, C.; Lotya, M.; Istrate, O. M.; King, P.; et al. Scalable Production of Large Quantities of Defect-Free Few-Layer Graphene by Shear Exfoliation in Liquids. *Nat. Mater.* **2014**, *13* (6), 624–630.

(29) Chen, J.; Shi, W.; Fang, D.; Wang, T.; Huang, J.; Li, Q.; Jiang, M.; Liu, L.; Li, Q.; Dong, L.; et al. A Binary Solvent System for Improved Liquid Phase Exfoliation of Pristine Graphene Materials. *Carbon*. **2015**, *94*, 405–411.

(30) Lin, S.; Dong, L.; Zhang, J.; Lu, H. Room-Temperature Intercalation and ~1000-Fold Chemical Expansion for Scalable Preparation of High-Quality Graphene. *Chem. Mater.* **2016**, *28* (7), 2138–2146.

(31) Geng, X.; Guo, Y.; Li, D.; Li, W.; Zhu, C.; Wei, X.; Chen, M.; Gao, S.; Qiu, S.; Gong, Y.; et al. Interlayer Catalytic Exfoliation Realizing Scalable Production of Large-Size Pristine Few-Layer Graphene. *Sci. Rep.* **2013**, *3*, 1–6.

(32) Matsumoto, M.; Saito, Y.; Park, C.; Fukushima, T.; Aida, T. Ultrahigh-Throughput Exfoliation of Graphite into Pristine “single-Layer” Graphene Using Microwaves and Molecularly Engineered Ionic Liquids. *Nat. Chem.* **2015**, *7* (9), 730–736.

(33) Liu, M.; Zhang, X.; Wu, W.; Liu, T.; Liu, Y.; Guo, B.; Zhang, R. One-Step Chemical Exfoliation of Graphite to ~100% Few-Layer Graphene with High Quality and Large Size at Ambient Temperature. *Chem. Eng. J.* **2019**, *355* (June 2018), 181–185.

(34) Park, K. H.; Kim, B. H.; Song, S. H.; Kwon, J.; Kong, B. S.; Kang, K.; Jeon, S. Exfoliation of Non-Oxidized Graphene Flakes for Scalable Conductive Film. *Nano Lett.* **2012**, *12* (6), 2871–2876.

(35) Wang, J.; Manga, K. K.; Bao, Q.; Loh, K. P. High-Yield Synthesis of Few-Layer Graphene Flakes through Electrolyte. *J. Am. Chem. Soc.* **2011**, *133*, 8888–8891.

(36) Yang, S.; Brüller, S.; Wu, Z. S.; Liu, Z.; Parvez, K.; Dong, R.; Richard, F.; Samori, P.; Feng, X.; Müllen, K. Organic Radical-Assisted Electrochemical Exfoliation for the Scalable Production of High-Quality Graphene. *J. Am. Chem. Soc.* **2015**, *137* (43), 13927–13932.

(37) Zhang, Y.; Xu, Y. Simultaneous Electrochemical Dual-Electrode Exfoliation of Graphite toward Scalable Production of High-Quality Graphene. *Adv. Funct. Mater.* **2019**, *1902171*, 1–14.

(38) Chen, C. H.; Yang, S. W.; Chuang, M. C.; Woon, W. Y.; Su, C. Y. Towards the Continuous Production of High Crystallinity Graphene via Electrochemical Exfoliation with Molecular in Situ Encapsulation. *Nanoscale*. **2015**, *7* (37), 15362–15373.

(39) Liu, J.; Poh, C. K.; Zhan, D.; Lai, L.; Lim, S. H.; Wang, L.; Liu, X.; Gopal Sahoo, N.; Li, C.; Shen, Z.; et al. Improved Synthesis of Graphene Flakes from the Multiple Electrochemical Exfoliation of Graphite Rod. *Nano Energy* **2013**, *2* (3), 377–386.

(40) Hummers, W. S.; Offeman, R. E. Preparation of Graphitic Oxide. *J. Am. Chem. Soc.* **1958**, *80* (6), 1339.

(41) Morales, G. M.; Schifani, P.; Ellis, G.; Ballesteros, C.; Martínez, G.; Barbero, C.; Salavagione, H. J. High-Quality Few Layer Graphene Produced by Electrochemical Intercalation and Microwave-Assisted Expansion of Graphite. *Carbon*. **2011**, *49* (8), 2809–2816.

(42) He, P.; Gu, H.; Wang, G.; Yang, S.; Ding, G.; Liu, Z.; Xie, X. Kinetically Enhanced Bubble-Exfoliation of Graphite toward High-Yield Preparation of High-Quality Graphene. *Chem. Mater.* **2017**, *29* (20), 8578–8582.

(43) Serrano, K.; Michaud, P. A.; Comninellis, C.; Savall, A. Electrochemical Preparation of Peroxodisulfuric Acid Using Boron Doped Diamond Thin Film Electrodes. *Electrochim. Acta*. **2002**, *48* (4), 431–436.

(44) Khamis, D.; Mahé, E.; Dardoize, F.; Devilliers, D. Peroxodisulfate Generation on Boron-Doped Diamond Microelectrodes Array and Detection by Scanning Electrochemical Microscopy. *J. Appl. Electrochem.* **2010**, *40* (10), 1829–1838.

(45) Michaud, P.; Mahé, E.; Haenni, W.; Perret, A.; Comminellis, C. Preparation of Peroxodisulfuric Acid Using Boron-Doped Diamond Thin Film Electrodes. *2007*, **3** (2), 77–79.

(46) Seiler, S.; Halbig, C. E.; Grote, F.; Rietsch, P.; Börrnert, F.; Kaiser, U.; Meyer, B.; Eigler, S. Effect of Friction on Oxidative Graphite Intercalation and High-Quality Graphene Formation. *Nat. Commun.* **2018**, **9** (1), 1–9.

(47) Eigler, S. Graphite Sulphate - A Precursor to Graphene. *Chem. Commun.* **2015**, **51** (15), 3162–3165.

(48) Bae, S. H.; Lee, Y.; Sharma, B. K.; Lee, H. J.; Kim, J. H.; Ahn, J. H. Graphene-Based Transparent Strain Sensor. *Carbon*. **2013**, **51** (1), 236–242.

(49) Hempel, M.; Nezich, D.; Kong, J.; Hofmann, M. A Novel Class of Strain Gauges Based on Layered Percolative Films of 2D Materials. *Nano Lett.* **2012**, **12** (11), 5714–5718.

(50) Carvalho, A. F.; Fernandes, A. J. S.; Leitão, C.; Deuermeier, J.; Marques, A. C.; Martins, R.; Fortunato, E.; Costa, F. M. Laser-Induced Graphene Strain Sensors Produced by Ultraviolet Irradiation of Polyimide. *Adv. Funct. Mater.* **2018**, **28** (52), 1–8.

(51) Kim, Y. J.; Cha, J. Y.; Ham, H.; Huh, H.; So, D. S.; Kang, I. Preparation of Piezoresistive Nano Smart Hybrid Material Based on Graphene. *Curr. Appl. Phys.* **2011**, **11** (1 SUPPL.), S350–S352.

(52) Wang, B.; Lee, B. K.; Kwak, M. J.; Lee, D. W. Graphene/Polydimethylsiloxane Nanocomposite Strain Sensor. *Rev. Sci. Instrum.* **2013**, **84** (10).

(53) Lee, Y.; Bae, S.; Jang, H.; Jang, S.; Zhu, S. E.; Sim, S. H.; Song, Y. Il; Hong, B. H.; Ahn, J. H. Wafer-Scale Synthesis and Transfer of Graphene Films. *Nano Lett.* **2010**, **10** (2), 490–493.

(54) Zhao, J.; He, C.; Yang, R.; Shi, Z.; Cheng, M.; Yang, W.; Xie, G.; Wang, D.; Shi, D.; Zhang, G. Ultra-Sensitive Strain Sensors Based on Piezoresistive Nanographene Films. *Appl. Phys. Lett.* **2012**, **101** (6).

(55) Eswaraiah, V.; Jyothirmayee Aravind, S. S.; Balasubramaniam, K.; Ramaprabhu, S. Graphene-Functionalized Carbon Nanotubes for Conducting Polymer Nanocomposites and Their Improved Strain Sensing Properties. *Macromol. Chem. Phys.* **2013**, **214** (21), 2439–2444.

(56) Boland, C. S.; Khan, U.; Backes, C.; O'Neill, A.; McCauley, J.; Duane, S.; Shanker, R.; Liu, Y.; Jurewicz, I.; Dalton, A. B.; et al. Sensitive, High-Strain, High-Rate Bodily Motion Sensors Based on Graphene-Rubber Composites. *ACS Nano*. **2014**, **8** (9), 8819–8830.

(57) Li, X.; Yang, T.; Yang, Y.; Zhu, J.; Li, L.; Alam, F. E.; Li, X.; Wang, K.; Cheng, H.; Lin, C. Te; et al. Large-Area Ultrathin Graphene Films by Single-Step Marangoni Self-Assembly for Highly Sensitive Strain Sensing Application. *Adv. Funct. Mater.* **2016**, **26** (9), 1322–1329.

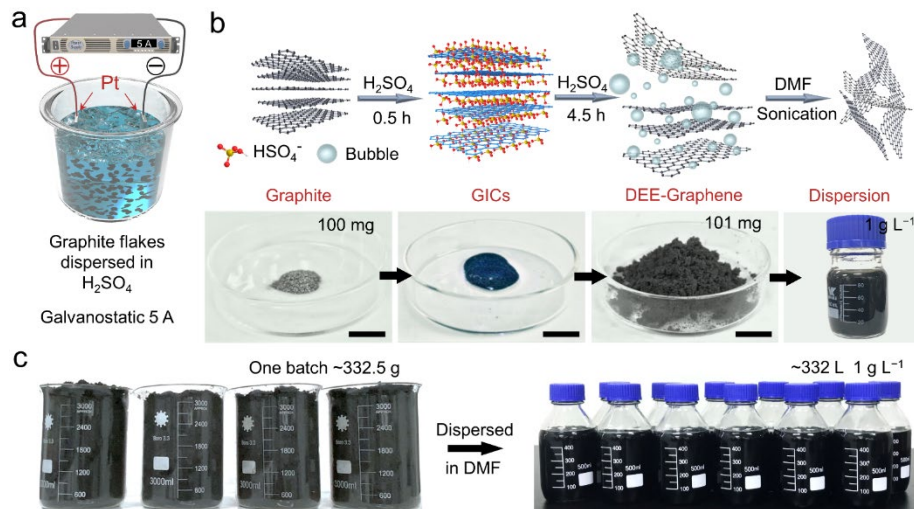


Figure 1. Processes and scalability of the DEE. (a) Schematic illustration of the DEE device. (b) The DEE procedures and corresponding products of every step (Scale bar:1 cm). (c) Massively prepared products in powder and dispersion forms.

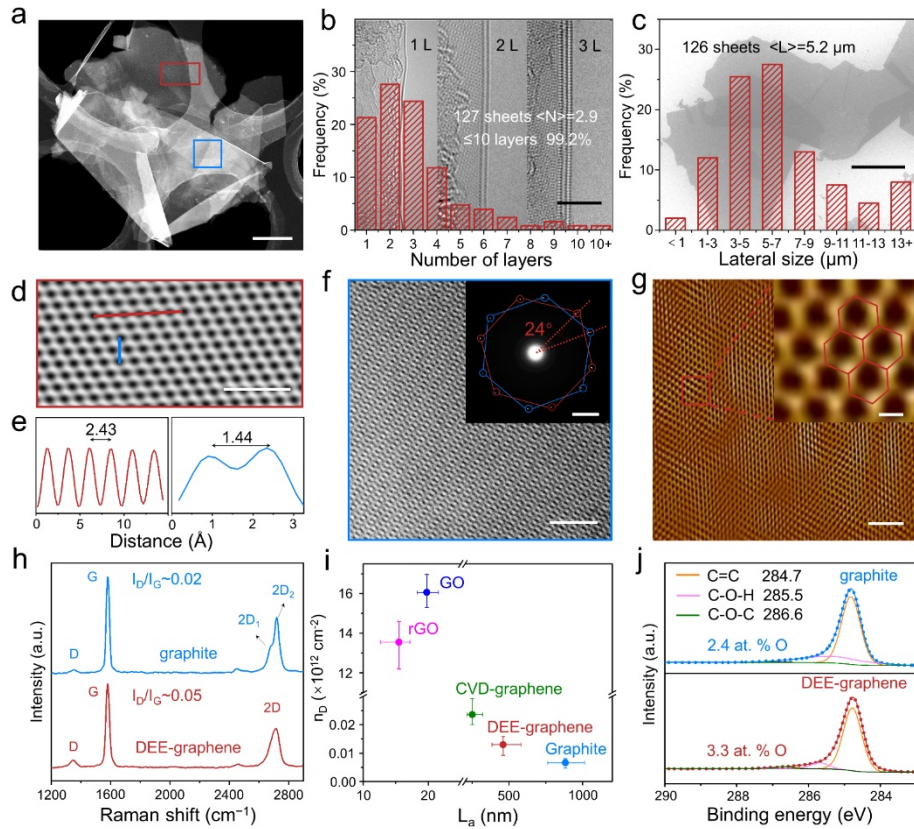


Figure 2. Morphology and chemical structure of the DEE-graphene. (a) The HAADF-STEM image of DEE-graphene (scale bar: 1 μ m). (b) HRTEM images and thickness histograms of the DEE-graphene (scale bar: 5 nm). (c) SEM image and lateral size histograms of the DEE-graphene sheet (scale bar: 2 μ m). (d, e) The filtered image (from the red rectangle in Figure 2a; scale bar: 1 nm) (d) and intensity analysis (along the red and blue line in Figure 2d) (e). (f) The HRTEM image and corresponding SAED pattern (from the blue rectangle in Figure 2a; scale bar: 2 nm, inset: 2 1/nm). (g) The STM image and locally magnified image of the DEE-graphene sheets (scale bar: 2 nm, inset: 2 \AA). (h) The Raman spectra of graphite and DEE-graphene. (i) Evolution of the n_D ratio versus the L_a of different types of graphene. (j) High-resolution C 1s spectra of graphite and DEE-graphene.

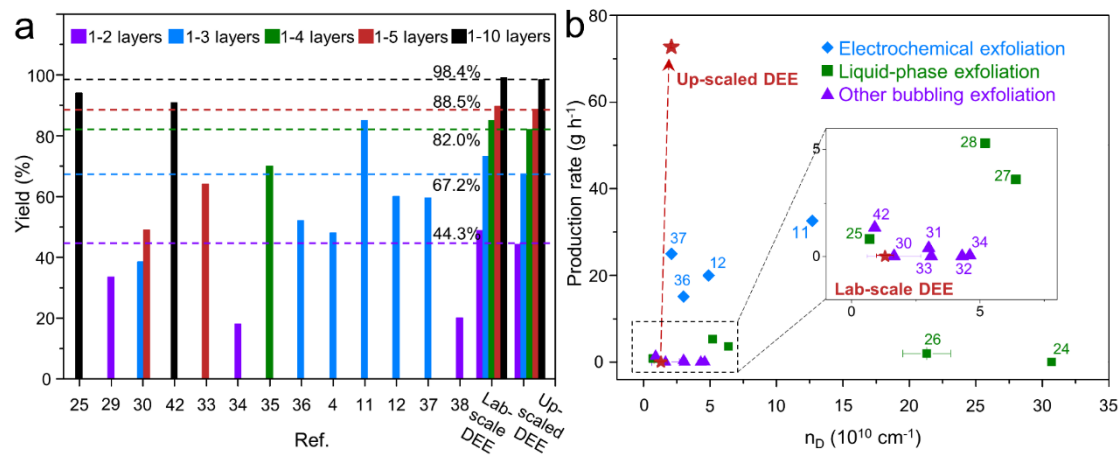


Figure 3. Yield (a), production rates and defect density (n_D) (b) of the various graphene materials prepared through top-down routes listed in Table S2 and S3.^{4,11,12,24–38,42}

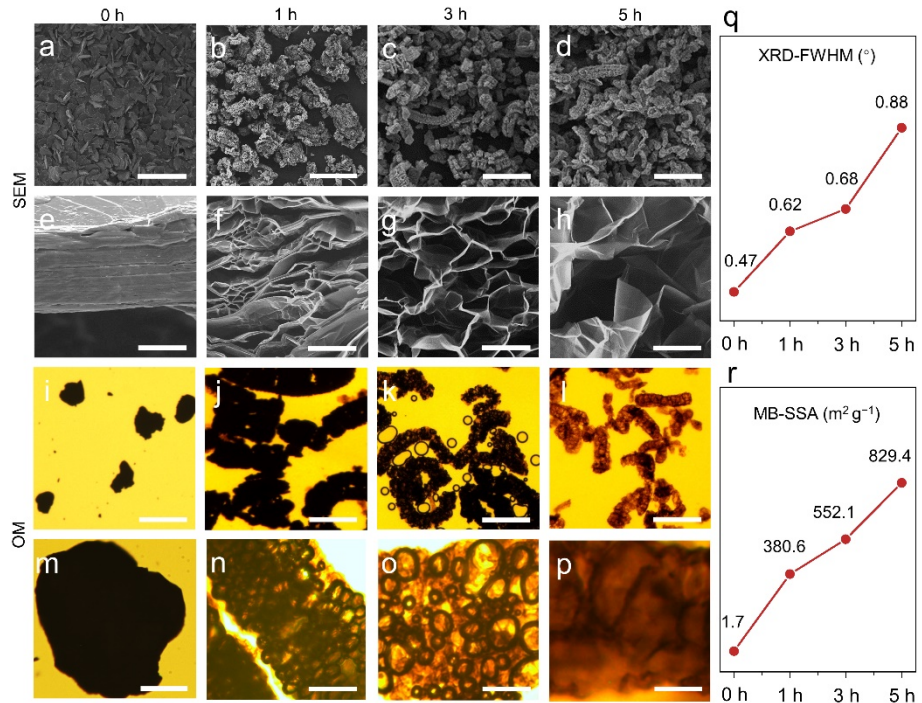


Figure 4. Morphology evolution from graphite precursor to the exfoliated products. (a-p) SEM and OM images of graphite (a, e, i, m), EG₁ (b, f, j, n), EG₃ (c, g, k, o) and EG₅ (d, h, l, p). The exfoliated products after different durations of electrochemical treatment are termed as EG_X (X represents the treatment time) (scale bars in a-d: 400 μ m; e-h: 5 μ m; i-l: 200 μ m and m-p: 20 μ m.). (q, r) The XRD-FWHM (q) and MB-SSA (r) of graphite and the exfoliated products.

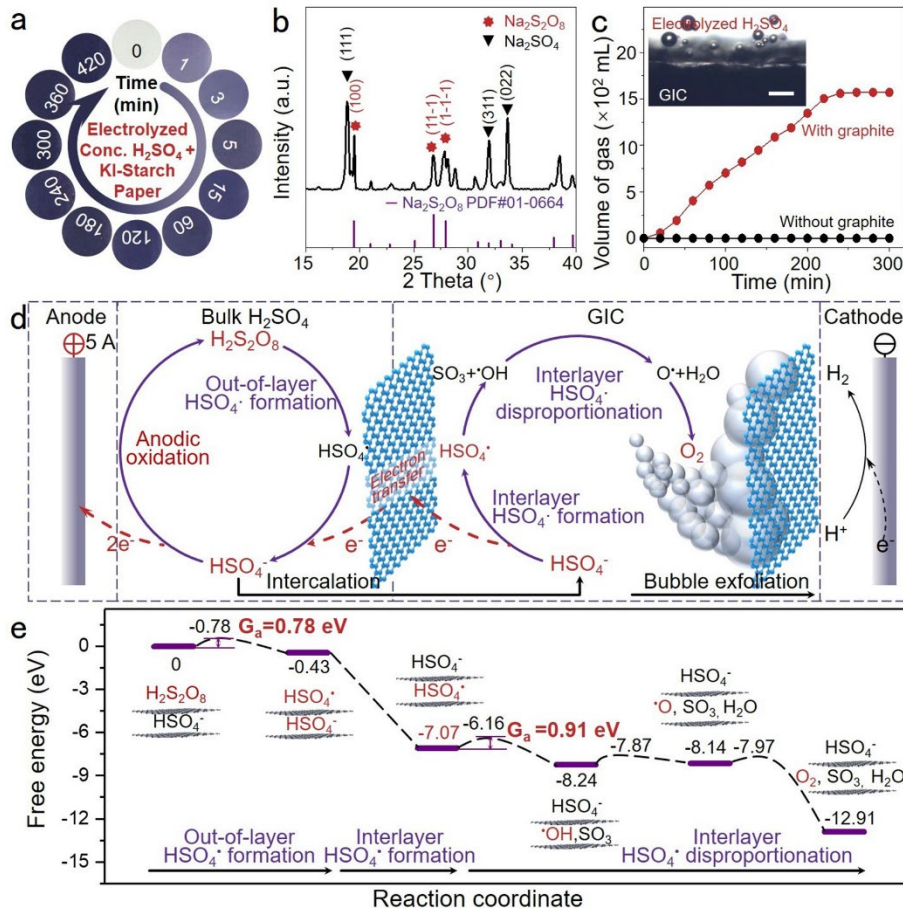


Figure 5. Mechanism analysis of the DEE. (a) KS test results of H_2SO_4 electrolyzed for different times. (b) XRD pattern of the solid extracted from the electrolyzed H_2SO_4 . (c) The gas release with and without the introduction of graphite into the electrolyzed H_2SO_4 (inset: bubbles appear at the interface of GIC and electrolyzed H_2SO_4 ; Scale bar: 200 μm). (d, e) The proposed reaction pathway (d) and corresponding energy profile for bubble exfoliation of graphite in DEE (e).

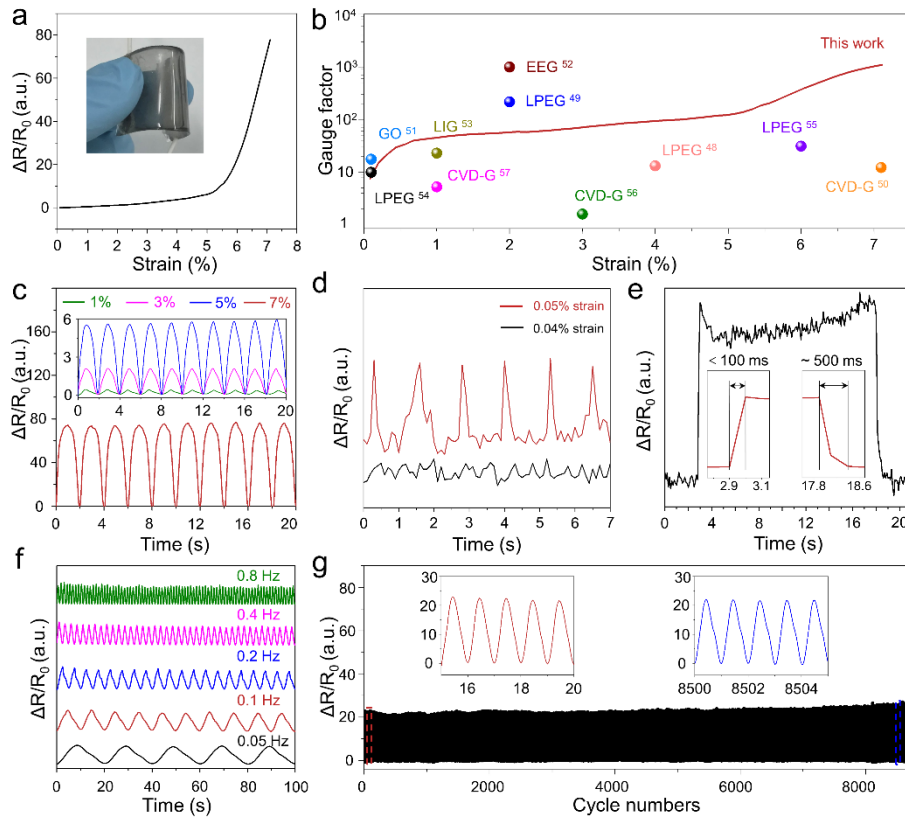


Figure 6. Properties of the DEE-graphene based strain sensors. (a) Relative resistance ($\Delta R/R_0$) response as a function of applied strain (inset: photograph of the strain sensor). (b) GF of the strain sensor at different strains and GF in previously reported works. (c) $\Delta R/R_0$ response at different strains (1%, 3%, 5% and 7%, 0.5 Hz). (d, e) The testing limit (d), response time and recovery time of the sensor (e). (f) $\Delta R/R_0$ response at different frequencies under 6% strain. (g) $\Delta R/R_0$ over 8600 cycles for 6% strain at 0.1 Hz (inset: the enlarged view of the records in the initial (left) and the last (right) 5 cycles). (LPEG: liquid-phase exfoliation graphene, EEG: electrochemical exfoliation graphene, GO: graphene oxide, LIG: laser-induced graphene, CVD-G: chemical vapor deposition grown graphene).

SUPPORTING INFORMATION

Delocalized Electrochemical Exfoliation toward High-throughput Fabrication of High-quality Graphene

Penglei Zhang^{1,2}, Peng He^{1,2,*}, Qingkai Yu³, Gang Wang⁴, Tao Huang^{1,2}, Siwei Yang^{1,2}, Xaosong Liu^{1,2,5}, Zhi Liu^{1,2,5}, Xiaoming Xie^{1,2,5}, Guqiao Ding^{1,2,*}

¹State Key Laboratory of Functional Materials for Informatics, Center for Excellence in Superconducting Electronics, Shanghai Institute of Microsystem and Information Technology, Chinese Academy of Sciences, 865 Changning Road, Shanghai 200050

²College of Materials Science and Opto-Electronic Technology, University of Chinese Academy of Sciences, Beijing 100049, P. R. China

³Ingram School of Engineering and MSEC, Texas State University, San Marcos, Texas 78666, United States

⁴Department of Microelectronic Science and Engineering, Faculty of Science, Ningbo University, Ningbo 315211, P. R. China

⁵School of Physical Science and Technology, ShanghaiTech University, Shanghai 200031, P. R. China

1. Experimental section

(1) Instrumentation.

A direct current (DC) electrochemical workstation (KEYSUGHT N5765A) was used as the power supply for the delocalized electrochemical exfoliation (DEE). Cooling water circulation machine (JULABO, F25) and magnetic stirring apparatus (IKA, C-MAG HS7) were used to control the temperature of the reaction system and disperse the graphite into the electrolyte. A bath sonicator (JP-040ST, 500W, 40KHz) was used to disperse the electrochemically treated products into DMF. High-resolution transmission electron microscopy (HRTEM) and high-angle annular dark-field scanning transmission electron microscopy (HAADF-STEM) analyses for microstructure were carried out on JEOL GRAND ARM at an accelerating voltage of 80 kV. The filtered images and intensity analyses results were obtained with Gatan DigitalMicrograph software. Scanning electron microscopy (SEM) images were obtained by TESCAN MIRA3. Atomic force microscopy (AFM) and scanning tunneling microscopy (STM) measurements were performed on Oxford Instruments Cypher S and STM measurements were performed in the constant current mode by applying a bias voltage to the sample. Raman spectra were obtained using RISE WITec with the laser wavelength of 532 nm. X-ray photoelectron spectroscopy (XPS) measurements were carried on Thermo Scientific Esca lab 250Xi. Fourier transform infrared spectroscopy (FT-IR) analyses were conducted on Nicolet IS10. UV-Vis absorbance spectra were obtained by Cary 100 to monitor the absorption process. Electron spin resonance (ESR) spectra were obtained using JEOL FA200. The gas chromatographic-mass spectra (GC-MS) were obtained using Thermo TSQ8000 Evo. The high-performance liquid chromatography-high resolution mass spectra (LC-MS) analyses were executed on Waters SQ Detector 2. Optical microscopy (OM) images were obtained using Caikon DCM 680C. X-ray diffraction (XRD) measurements were performed on Bruker D8 ADVANCE X-ray diffractometer with a monochromatic source of Cu K α 1 radiation at 1.6 kW (40 kV, 40 mA). A rotary evaporator (SHB-III) was used to evaporate water and extract solid products from the electrolyzed and neutralized H₂SO₄. A high-precision motorized linear stage (Wellknown, DZZXT300MA06-PC130-1) was used to implement strain load to the strain sensors (displacement resolution of 2.5 μ m).

(2) Materials

Graphite flakes (300 mesh) were purchased from Qingdao Xinghe Graphite Co., Ltd.. HOPG was purchased from Jiangsu XFNANO Material Co., Ltd.. Concentrated sulfuric acid (H₂SO₄, 98%, AR), dimethyl sulfoxide (DMSO, \geq 99.0%, AR), 5,5-dimethyl-1-pyrroline N-Oxide (DMPO, 97%), N,N-dimethylformamide (DMF, 99.5%, AR), methylene blue (MB, BS), polydimethylsiloxane (PDMS) and ammonia solution (NH₄OH, 25%, AR) were purchased from Sinopharm Chemical Reagent Co., Ltd.. KI-Starch (KS) papers were purchased from Shanghai SSS reagent Co., Ltd.. The deionized water (DI water, resistivity \sim 18.2 M Ω cm at 25°C) used in all experiments was made by a Millipore purification system (LD, Mighty-10). All raw materials and reagents were used without further purification.

(3) Methods

Preparation of high-quality graphene by DEE: Firstly, electrolyte solution containing 100 mL H₂SO₄ and 100 mg graphite flakes (300 mesh) were mixed by magnetic stirring (300 r/min) in a glass reactor equipped with temperature-controlling water circulation (25 °C). Then, two Pt foils

(10 cm×1 cm) acting as electrodes were vertically inserted into the electrolyte solution (2 cm apart and 3 cm immersed) and applied with a constant current (DC, 5 A) to initiate the electrochemical treatment. Five hours later, the obtained reaction slurry was purified to get the powder (101 mg) after consecutive filtration using a filter (300 mesh), repeated rinsing with water until the pH of the filtrate became neutral, and complete drying in an oven (60 °C, 7 h). Finally, the powder was bath-sonicated (500 W, 25 °C, 10 min) in N,N-dimethylformamide (DMF) to obtain the dispersion of high-quality graphene (DEE-graphene).

Up-scaled DEE for high-quality graphene fabrication: 330 g graphite flakes (300 mesh) and 6 L H₂SO₄ were mixed by a magnetic stirring (400 r/min) in a glass reactor (12 L) equipped with temperature-controlling water circulation (25 °C). The ring-shaped anode (80 cm×20 cm) centered by a flat cathode strip (20 cm×3 cm) were vertically inserted into the electrolyte solution (12 cm apart and 10 cm immersed). A current of 20 A (DC) was applied to conduct the up-scaled DEE. After about 4.5 h, the slurry was collected by a filter (300 mesh), repeated rinsing with water until the pH of the filtrate became neutral, and complete drying in an oven (60 °C, 7 h) to get the powder. And the uniform DEE-graphene dispersion can be obtained by bath sonication (500 W, 25 °C, 10 min) of the powder in DMF.

Fabrication of stain sensors: The strain sensors with planar geometry were fabricated by coating the flexible polydimethylsiloxane (PDMS) substrate with graphene sheets. An interfacial assembly technique was used to assemble high-quality graphene sheets into continuous graphene films. Specifically, 20 mL graphene dispersion (0.1 mg/mL in DMF) was dropped into a beaker (8 cm in diameter) containing 300 mL DI water. Benefiting from their hydrophobicity, graphene sheets assembly into interconnecting films at the water-air interface when the DMF as the solvent dissolves into the water. The area covered by graphene films became bigger with the increasing loading of graphene dispersion. Subsequently, the self-assembled graphene film floating on the liquid surface was transferred onto a PDMS substrate via dip coating (Figure S24a) and completely dried in an oven (50 °C, 24 h). Finally, both sides of the obtained graphene/PDMS strip were applied with conductive silver paint to form electrodes that can be connected by copper wires to the test workstation for performance assessment.¹

2. Supporting data for the processes of DEE

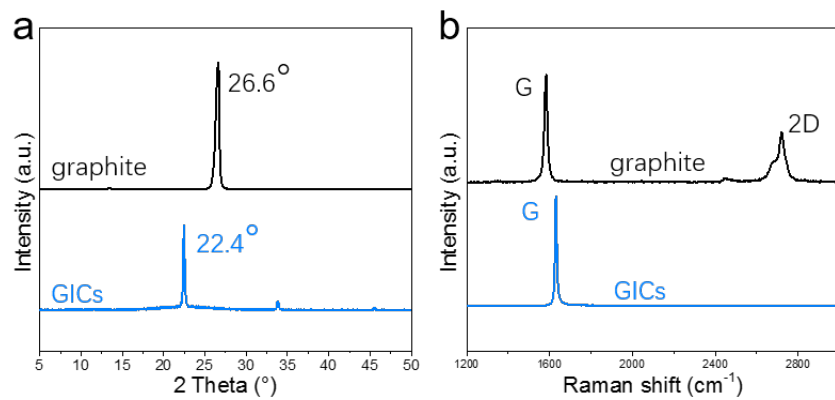


Figure S1. Structure characterizations for the intermediate products of DEE showing the formation of 1-GIC. (a, b) The XRD patterns (a) and Raman spectra (b) of the intermediate products and graphite.

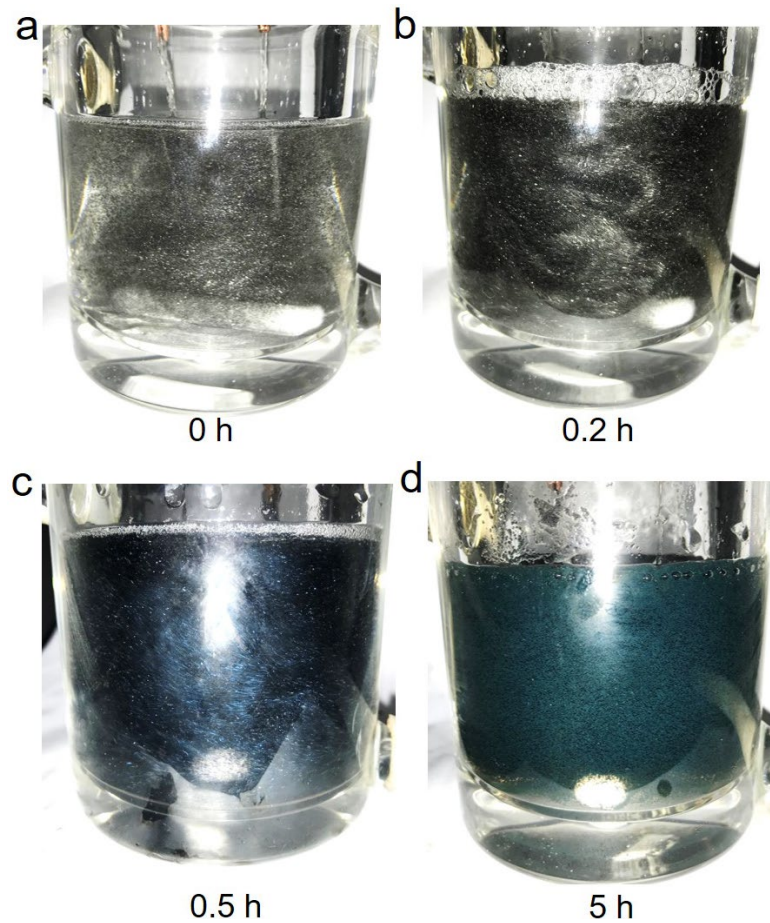


Figure S2. Color change of the bulk-phase electrolyte during DEE in different time. (a) 0 h; (b) 0.2 h; (c) 0.5 h; (d) 5 h.

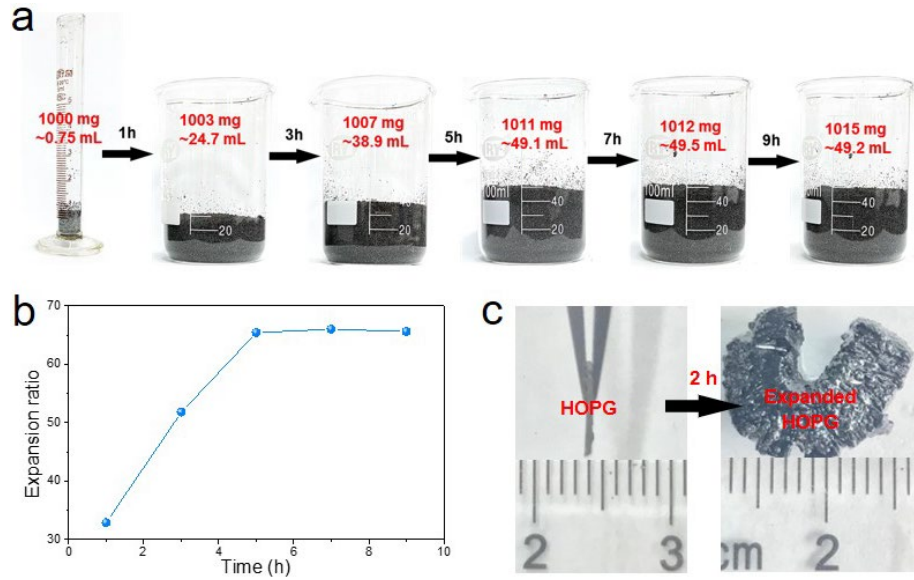


Figure S3. Volume expansion of the graphite during DEE. (a, b) Volume change of 1 g graphite after different durations of electrochemical treatment (a) and corresponding expansion ratios (b). (c) Photographs of HOPG strips before and after 2-hour DEE.

The volume of the expanded graphite after 5-hour DEE is approximately 65 times that of its precursor graphite flakes (Figure S3a). Further increasing the electrolysis time resulted in no obvious increase of volume and expansion ratio (Figure S3b), from which we determined 5 hours to be the optimal duration of lab-scale DEE. HOPG as a big graphite block also undergone notable color change and volume expansion when put it in the electrochemical cell for 2 h, which visually shows the exfoliation effect of DEE (Figure S3c). It should be noted that directly stirring graphite flakes or HOPG in the electrolyte cannot initiate the color change or the volume expansion, which highlights the role of the applied DC bias for graphite exfoliation.

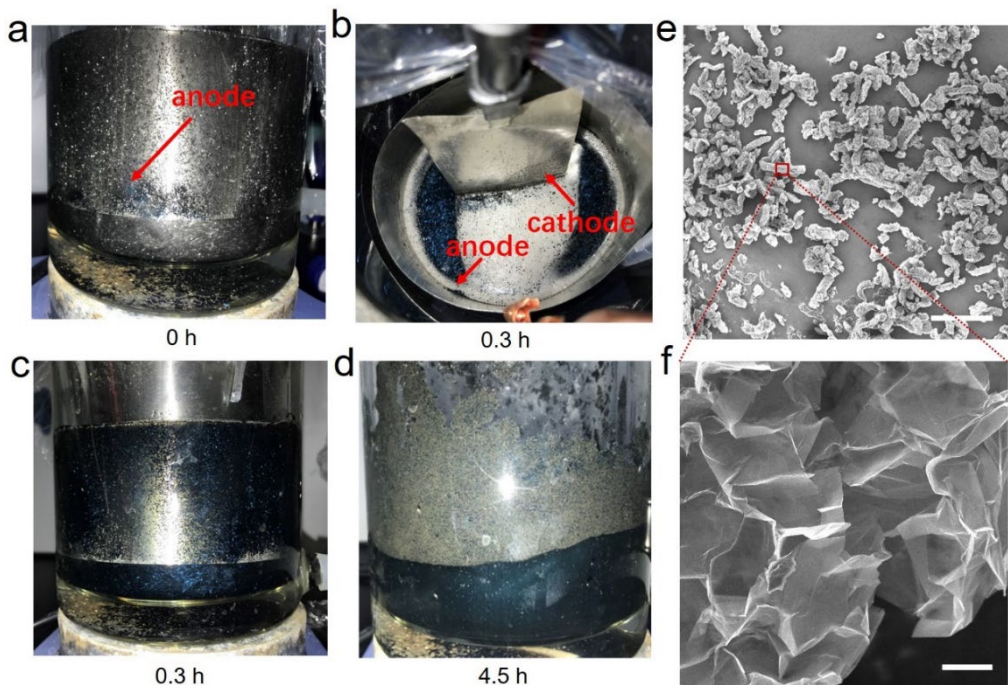


Figure S4. Configuration of the electrodes for the up-scaled DEE and corresponding product.

(a, b) Photographs of the ring-shaped anode (a) centered by a flat cathode strip (b). (c, d) Photographs showing the varying color of the bulk-phase electrolyte during up-scaled production, which is similar to the lab-scale case. (e, f) The SEM image (e) and locally magnified image (f) of the up-scaled DEE product. (Scale bar in e: 400 μ m and f: 5 μ m)

Similar to the lab-scale preparation, both color change and volume expansion can be observed during the up-scaled DEE. The resulting powder has a similar morphology to that of the lab-scale preparation (Figure S4e and f). Volume expansion ratio after 4.5 h of electrochemical treatment is determined to be \sim 63, indicating a deep exfoliation of the graphite flakes in the bulk-phase during the up-scaled fabrication.

3. Supporting data for the characterizations of DEE-graphene

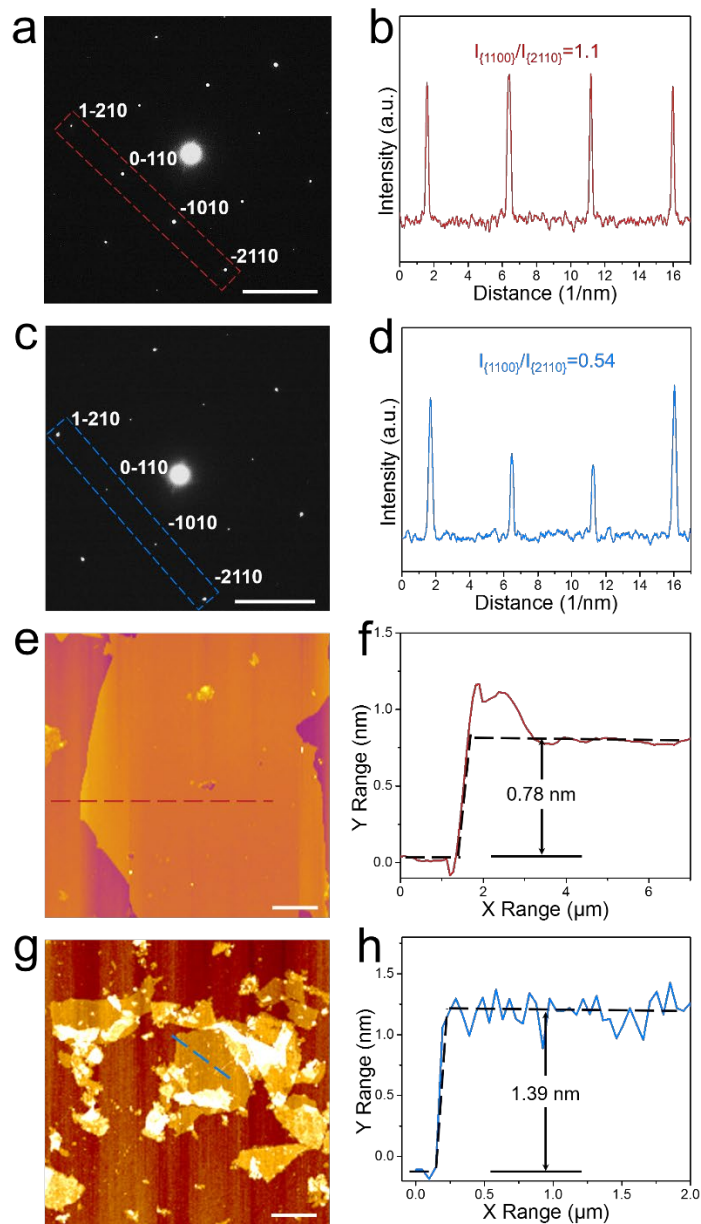


Figure S5. Characterizations showing the presence of single- and few-layer sheets in DEE-graphene. a–d, The SEAD diffraction patterns (a, c) and the diffracted intensity taken along the (1–210) to (−2110) axis (b, d). (Scale bars in a and c: 5 1/nm.). (e–h) Typical AFM images (e, g) and topological height profiles along the dotted line in Figure S5e and g (f, h). (Scale bars in e and g: 1 μ m)

As shown in Figure S5a and b, the $\{1100\}$ spots are more intense than the $\{2110\}$ spots ($I_{\{1100\}}/I_{\{2110\}}=1.1$), demonstrating the presence of single-layer graphene. In contrast, more intense $\{2110\}$ spots than $\{1100\}$ spots ($I_{\{1100\}}/I_{\{2110\}}=0.54$) is observed as presented in Figure S5c and d, revealing the presence of few-layer graphene in the sample.² Besides, typical AFM images and

height profiles show sheets of 0.78 nm and 1.39 nm in thickness (Figure S5e–h), which also reveals the presence of single- and bi-layer the graphene.³

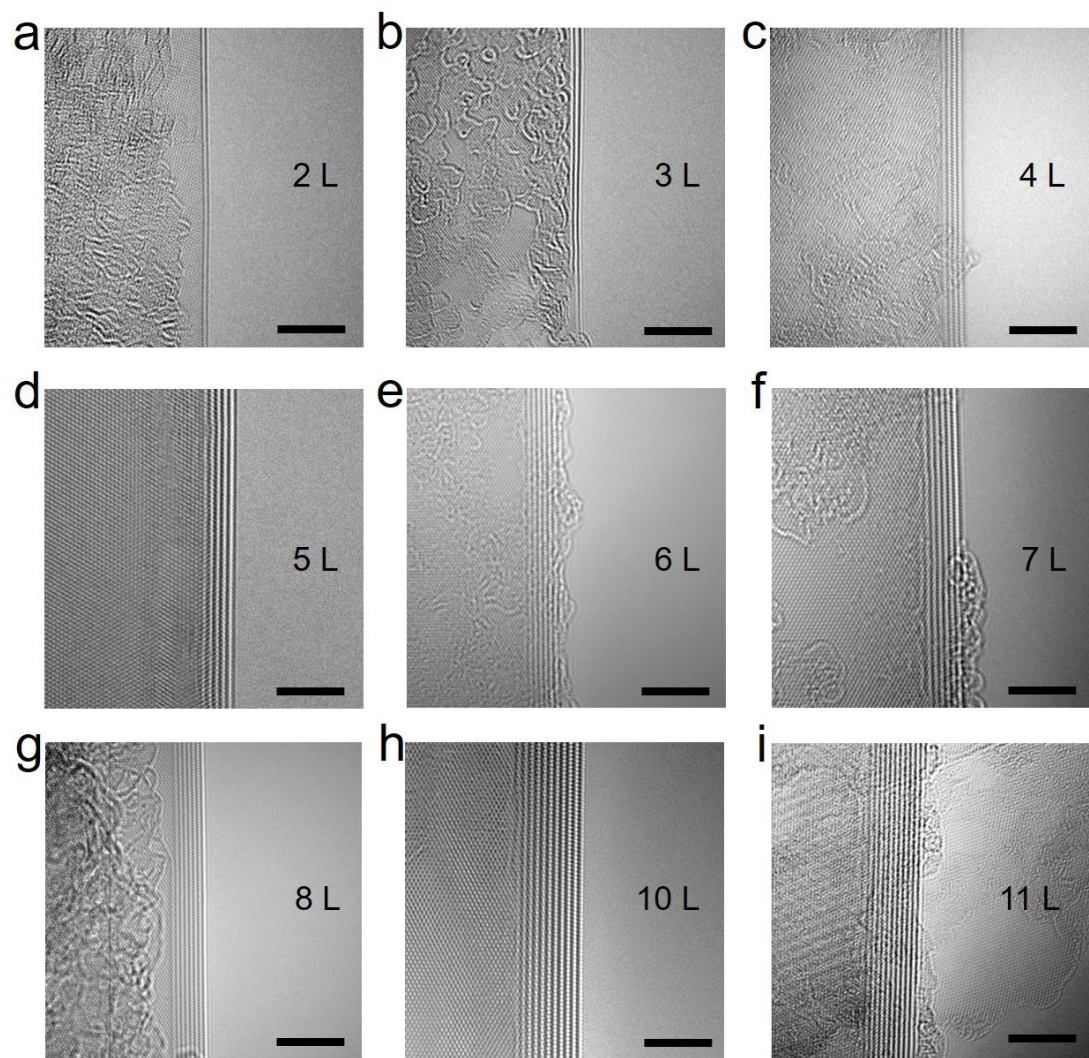


Figure S6. Typical HRTEM images of the DEE-graphene sheets at folded edges. (Scale bars in a–i: 5 nm)

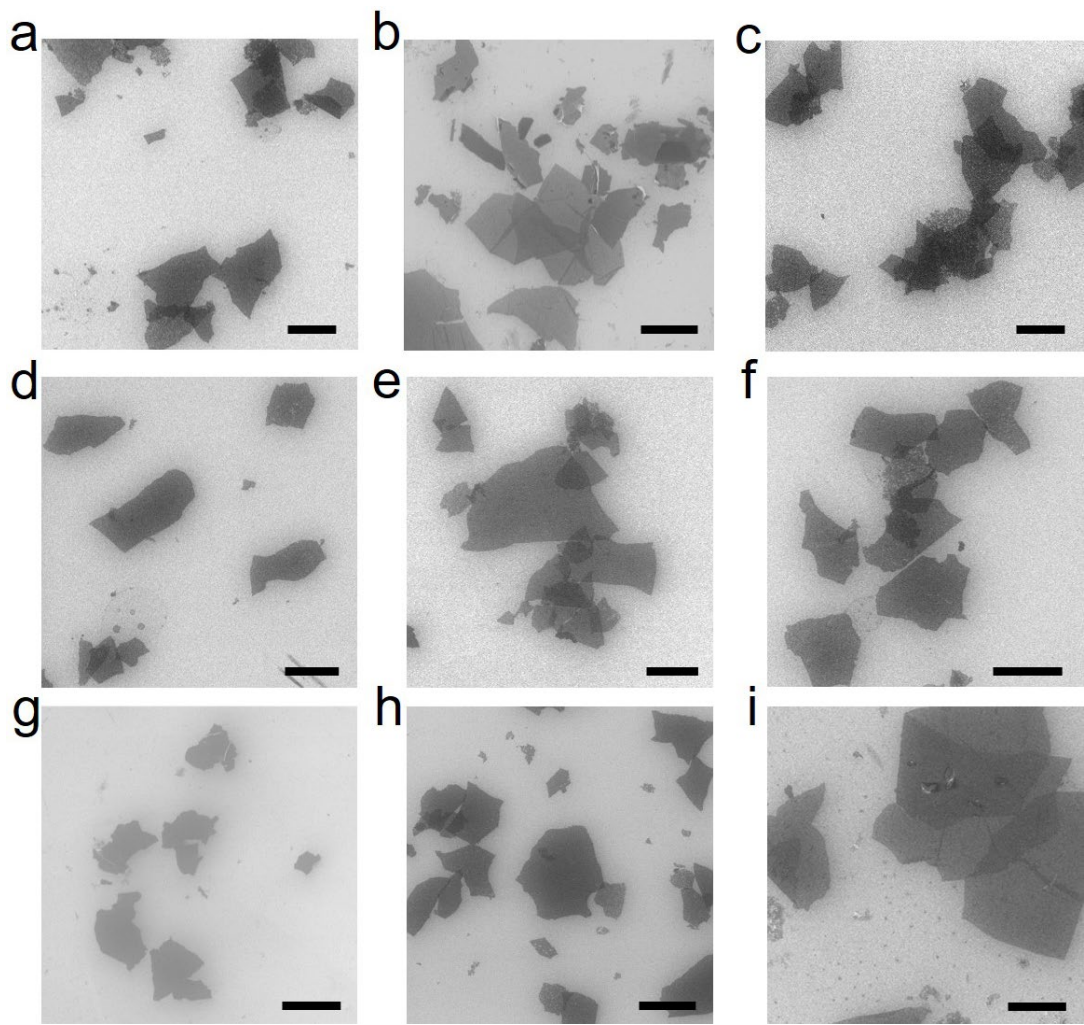
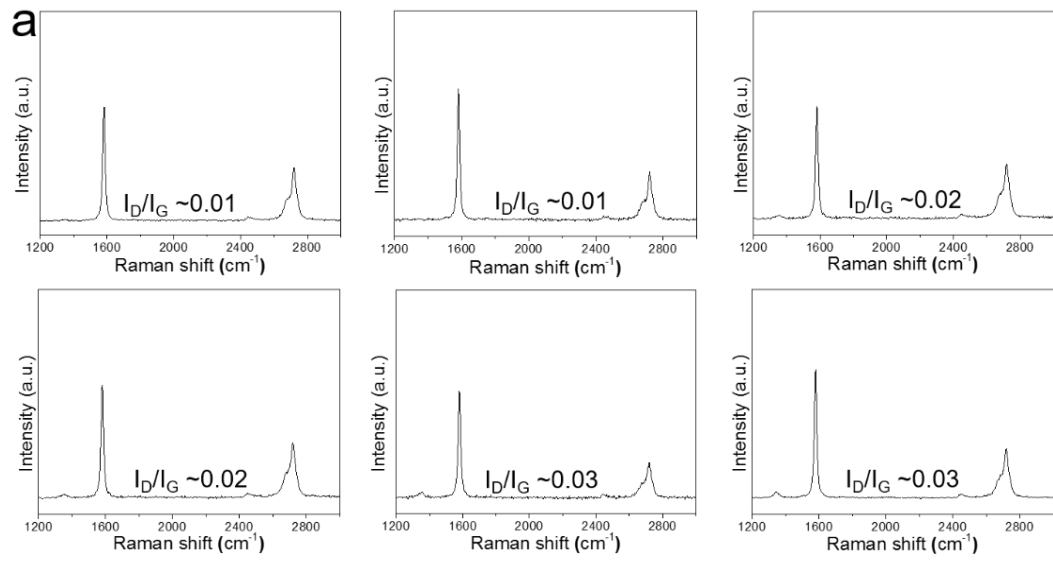


Figure S7. Typical SEM images of DEE-graphene sheets. (Scale bars in a–i: 5 μm)



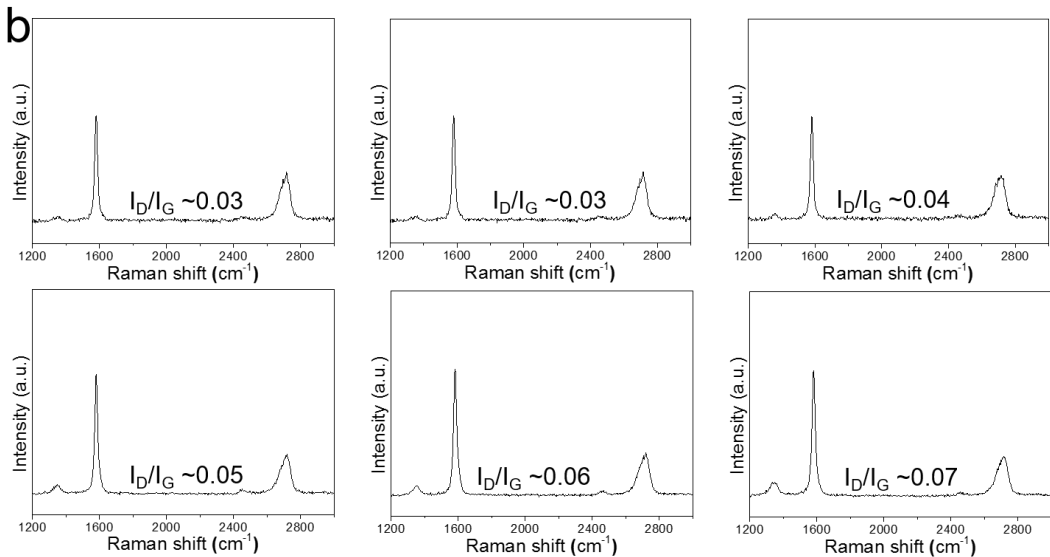


Figure S8. Typical Raman spectra of graphite precursor (a) and the DEE-graphene (b). (I_D : the intensity of Raman D band; I_G : the intensity of Raman G band)

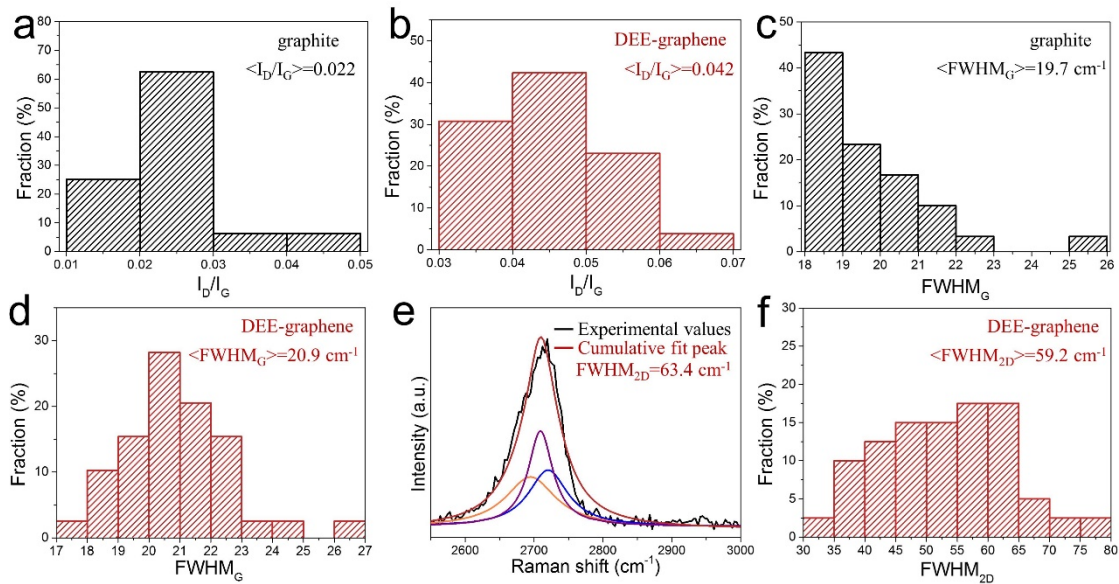


Figure S9. Raman data of DEE-graphene and graphite precursor. Histograms of Raman I_D/I_G of graphite (a) and DEE-graphene (b). Full width at half maximum of Raman G band (FWHM_G) of graphite (c) and the DEE-graphene (d). (e) Raman 2D band of DEE-graphene and its Lorentzian fit. (e) Histograms of Raman FWHM_{2D} of DEE-graphene.

The DEE-graphene has an I_D/I_G value close to that of the graphite precursor but smaller than the graphene prepared by other methods (Figure S9a, b, Table s2 and s3),^{9–13, 15–17, 20–22, 25–29, 31, 33–34} which indicates the low defect density in the DEE-graphene. The FWHM_G is sensitive to the structure disorder and generally increases with disorder.⁴ So, the close FWHM_G value of the DEE-graphene (20.9 cm^{-1}) to that of the graphite precursor (19.7 cm^{-1}) also revealed the preserved structure integrity during DEE in the bulk-phase (Figure S9c and d). It is well established that FWHM_{2D} value can be used as an indicator of graphene thickness. Generally, FWHM_{2D} range in

30–45 cm^{-1} for single-layer graphene, 45–60 cm^{-1} for bi-layer graphene and 60–75 cm^{-1} for tri-layer graphene.⁵ For DEE-graphene, a distribution of $\text{FWHM}_{2\text{D}}$ in the range from 30 to 80 cm^{-1} (Figure S9e and f) and an average of 59.2 cm^{-1} reveal the presence of single- and few-layer graphene in DEE product.

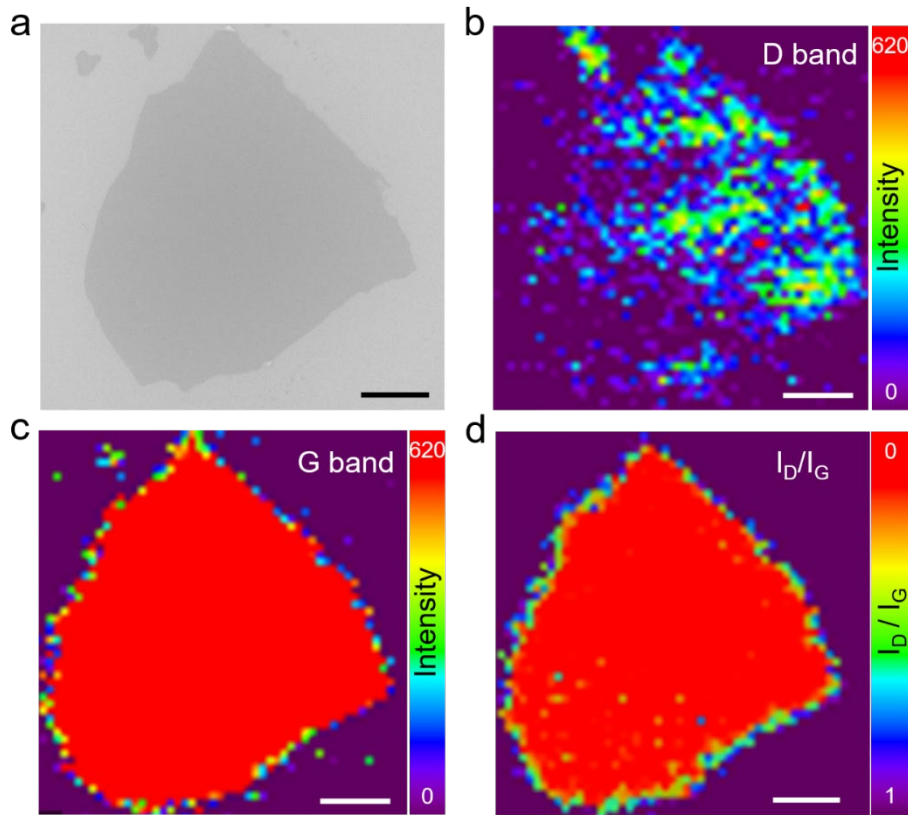


Figure S10. Raman mapping analyses of the DEE-graphene. (a) The SEM image of the DEE-graphene sheet. The Raman mapping of I_D (b), I_G (c) and I_D/I_G (d) of the DEE-graphene. (Scale bars in a–d: 1 μm)

For a single DEE-graphene sheet, Raman mapping reveals small and uniformly distributing I_D/I_G values in the basal plane. Relatively large I_D/I_G values are found in the edge areas, which should be the main structure defects in the DEE-graphene (Figure S10b–d).

Based on statistical average of I_D/I_G , $\text{FWHM}_{2\text{D}}$ and FWHM_G , we can obtain the crystalline quality parameters of DEE-graphene and graphite precursor as presented in Table S1 according to the correlations described in Note S1.

Table S1. Crystalline quality parameters of the DEE-graphene, graphite, CVD-G,⁶ GO⁷ and rGO.⁸

Materials	I_D/I_G	FWHM_G (cm^{-1})	L_a (nm)	L_D (nm)	n_D (10^{12} cm^{-2})
Graphite	0.022	19.7	867.91	69.02	0.0067
CVD-G	0.080	21.1	240.34	10.89	0.024
rGO	1.218	123.3	15.80	1.52	13.759
GO	1.038	155.2	18.53	1.44	15.393

DEE-graphene	0.042	20.9	459.10	50.15	0.013
--------------	-------	------	--------	-------	-------

CVD-G: graphene prepared by chemical vapor deposition

rGO: reduced graphene oxide

GO: graphene oxide

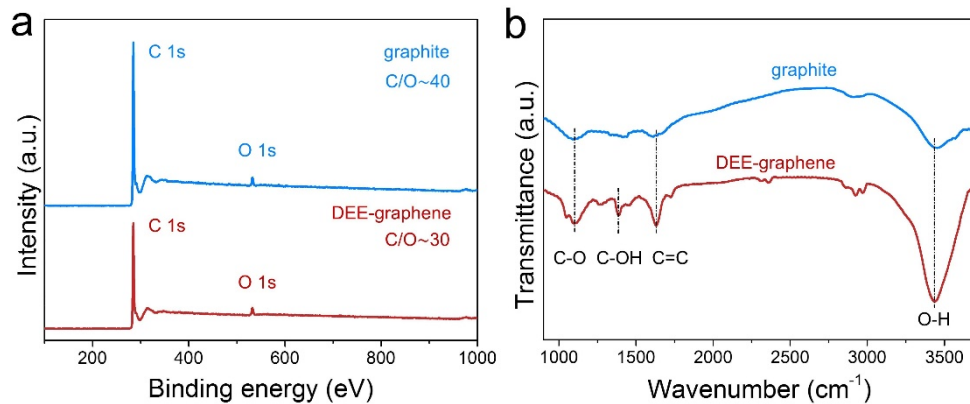


Figure S11. Chemical Structure of the DEE-graphene and the graphite precursor. (a, b) XPS survey spectra (a) and FT-IR spectra (b) of DEE-graphene and graphite.

The DEE-graphene sheets show a carbon-to-oxygen ratio (C/O, Figure S11a) of 30, which is larger than most graphene prepared by other methods (Table S2 and S3).^{15, 20, 26–29, 34, 35} This data, together with functional groups of low oxidation presence (C-O (1104.1 cm⁻¹), C-OH (1385.6 cm⁻¹), C=C (1626.6 cm⁻¹) and O-H (3435.6 cm⁻¹)) revealed by the FT-IR spectrum (Figure S11b), indicate that the DEE processing does not generate excess structural defects.

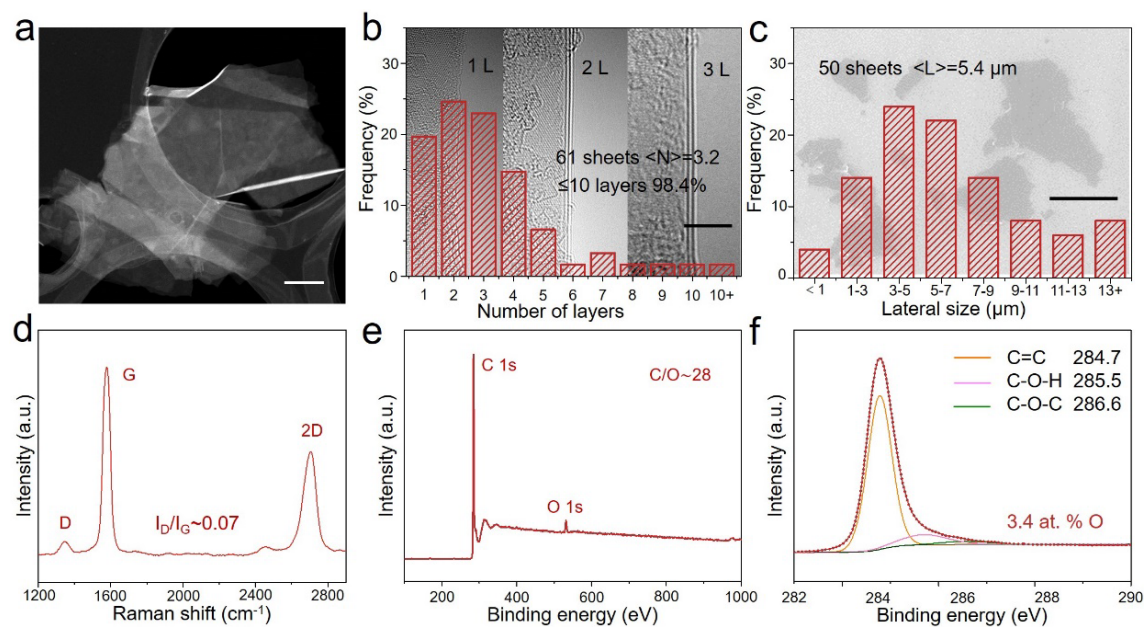


Figure S12. Characterizations of the graphene prepared from the up-scaled DEE. (a–f) The HAADF-STEM image (a), typical HRTEM images and the number of layers histogram (b), typical SEM image and lateral size histogram (c), Raman spectra (d), XPS survey spectra (e) and High-

resolution C 1s spectra (f) of up-scaled DEE-graphene. (Scale bar in a: 500 nm; b: 5 nm and d: 5 μ m.)

1 Table S2. Comparison of DEE and other top-down methods on reaction conditions, production rates and the crystal quality of the corresponding graphene.

Reaction condition		Thickness	C/O ratio	Density of defects (n _D , 10 ¹⁰ cm ⁻²)	Production rate (g h ⁻¹)	Yield	Ref.
Intercalation step	Exfoliation step						
-	Sonication in solution (sodium cholate), 1 h	Average 1.1 nm (1–2 layers)	NA	30.7 # (I _D /I _G ~0.93; FWHM _G ~26 cm ⁻¹)	0.018 #	NA	9
-	Grinding the mixture of expanded graphite and oxalic acid, 12 h	<10 layers	NA	0.7 # (I _D /I _G ~0.025; FWHM _G ~27 cm ⁻¹)	0.83 #	94%	10
-	Wet milling exfoliation with yttria stabilized zirconia acting as grinding media, 3 h	Average 2.7 nm (2–3 layers)	NA	19.5–23.1 # (I _D /I _G ~0.6–0.7; FWHM _G ~19 cm ⁻¹)	1.5–2.5 #	NA	11
-	High-speed laminar flow exfoliation in nonionic surfactant	Average 4.1 layers	NA	6.4 # (I _D /I _G ~0.21; FWHM _G ~29 cm ⁻¹)	3.6	18%	12
-	Shear exfoliation in surfactant solution	5–8 layers	NA	5.2 # (I _D /I _G ~0.17; FWHM _G ~24 cm ⁻¹)	5.3	3%	13
-	Sonicate in DMF/NBA solution, >2 h	33.5% 1–2 layers	NA	NA	9.5	NA	14
CrO ₃ +concentrated HCl @ room temperature, 2 h	H ₂ O ₂ (30%) @room temperature, 24 h	70% 1–5 layers	28	0.6–2.7 # (I _D /I _G ~0.02–0.09; FWHM _G ~25 cm ⁻¹)	0.027 #	70%	15
FeCl ₃ (gas) @380 °C, 24 h	H ₂ O ₂ (30%) @room temperature	<2 nm (2–3 layers)	NA	3.0 # (I _D /I _G ~0.1; FWHM _G ~23 cm ⁻¹)	~0.4 #	NA	16
Concentrated H ₂ SO ₄ +Na ₂ S ₂ O ₈ @25 °C, 10 min	Concentrated H ₂ SO ₄ +Na ₂ S ₂ O ₈ @80 °C, 30 min	1–10 layers	NA	0.9 # (I _D /I _G ~0.03; FWHM _G ~26 cm ⁻¹)	1.36 #	90.8%	17
H ₂ SO ₄ +(NH ₄) ₂ S ₂ O ₈ +oleum @ room temperature, 3–4 h		10–35 nm (30–103 layers)	NA	NA	NA	~100%	18
Concentrated H ₂ SO ₄ +Na ₂ S ₂ O ₈ @ room temperature, 3 h		10–20 nm (14–29 layers)	NA	NA	0.33 #	100%	19

Ionic liquid with microwave-assisted, 30 min	95% 1 layer	30	4.3 [#] ($I_D/I_G \sim 0.14$; $FWHM_G \sim 19 \text{ cm}^{-1}$)	0.023 [#]	93%	20
Peroxyacetic acid (CH_3COOOH) and H_2SO_4 binary-component system, 4 h	Average <5 layers	NA	3.1 [#] ($I_D/I_G \sim 0.102$; $FWHM_G \sim 24 \text{ cm}^{-1}$)	0.025 [#]	~100%	21
Ternary $\text{KCl}-\text{NaCl}-\text{ZnCl}_2$ eutectic salt 350 °C, 10 h	75% 0.4-10 nm (1-20 layers)	NA	4.6 [#] ($I_D/I_G \sim 0.15$; $FWHM_G \sim 18 \text{ cm}^{-1}$)	0.06 [#]	~60%	22
Grinding in the mixture of NaCl crystallites, oleum and TBA, >24 h	90% 1 layer	NA	NA	1.04×10^{-4} [#]	100%	23
NaK ₂ and graphite mixt @ room temperature with intermittent agitation	2-150 nm (2-214 layers)	NA	NA	0.9	NA	24
DC 5 A, H_2SO_4 @ room temperature, 5 h	Average 2.9 layers (89.8% ≤5 layers; 21.3% 1 layer)	30	1.3 ($I_D/I_G \sim 0.042$; $FWHM_G \sim 20.9 \text{ cm}^{-1}$)	0.02	99.2% (1-10 layers)	Lab-scale DEE
DC 20 A, H_2SO_4 @ room temperature, 4.5 h	Average 3.2 layers (88.5% ≤5 layers; 19.7% 1 layer)	28	2.1 ($I_D/I_G \sim 0.07$; $FWHM_G \sim 31.0 \text{ cm}^{-1}$)	72.7	98.4% (1-10 layers)	Up-scaled DEE

2 NA: Not applicable.

3 [#] Estimated from the data provided in the references.

4

5 Table S3. Comparison of DEE and other electrochemistry methods on reaction conditions, production rates and the crystal quality of the corresponding graphene.

6

Electrode		Electrolyte	Thickness	Lateral size	C/O ratio	Density of defects (n _D , 10 ¹⁰ cm ⁻²)	Production rate (g h ⁻¹)	Yield	Ref.
Anode	Cathode								
Graphite foil	Pt	Propylene carbonate + Li ⁺	<5 layers	1-2 μ m	NA	3.0 # (I _D /I _G ~0.1; FWHM _G ~29 cm ⁻¹)	NA	>70%	25
Graphite foil	Pt	(NH ₄) ₂ SO ₄ + antioxidants	52% 1-3 layers	5-10 nm	25.3	3.0 # (I _D /I _G ~0.1; FWHM _G ~23 cm ⁻¹)	~15.1	~75%	26
Graphite foil	Pt	0.1M H ₂ SO ₄	80% 1-3 layers	NA	12.3	12.6 # (I _D /I _G ~0.4; FWHM _G ~27 cm ⁻¹)	NA	>60%	27
Graphite foil	Pt	0.1M (NH ₄) ₂ SO ₄	85% \leq 3 layers	80% 5 μ m	17.2	12.7 # (I _D /I _G ~0.41; FWHM _G ~29 cm ⁻¹)	32.6	>85%	28
Graphite foil	Graphite foil	TBA·HSO ₄	75% 1-4 layers	5 μ m	21.2	4.9 # (I _D /I _G ~0.16; FWHM _G ~31 cm ⁻¹)	20	80%	29
Graphite rod	Pt	Oxalic acid solution	80% 4-8 nm (5-12 layers)	NA	NA	NA	NA	50%	30
Graphite foil	Pt	Glycine+H ₂ SO ₄	2-5 layers	NA	NA	23.1 # (I _D /I _G ~0.7; FWHM _G ~30 cm ⁻¹)	NA	NA	31
Graphite foil	Pt	Dilute H ₂ SO ₄	2 layers	NA	NA	NA	NA	5-8 wt%	32
Graphite foil	Pt	C ₂ O ₄ H ₂ +H ₂ O ₂	75% 3-5 layers	78.1% 2-6 μ m,	NA	00.6 # (I _D /I _G ~0.022; FWHM _G ~24 cm ⁻¹)	NA	27%	33
Graphite flakes	Graphite flakes	TBA·ClO ₄ + propylene carbonate	70% 1-3 layers	1-5 μ m	21.37	2.1 # (I _D /I _G ~0.071; FWHM _G ~19 cm ⁻¹)	25	85 % (cathode) 48% (anode)	34
Graphite plate	Graphite plate	H ₂ SO ₄ +melamine additives	80% <3 layers	18 μ m	26.17	NA	1.5	25 wt%	35
Pt	Pt	H ₂ SO ₄	Average 2.9 layers (89.8% \leq 5 layers; 21.3% 1 layer)	Average 5.2 μ m	30	1.3 (I _D /I _G ~0.042; FWHM _G ~20.9 cm ⁻¹)	0.02	99.2% (1-10 layers)	Lab-scale DEE
			Average 3.2 layers (88.5% \leq 5 layers; 19.7% 1 layer)	Average 5.4 μ m	28	2.1 (I _D /I _G ~0.07; FWHM _G ~31 cm ⁻¹)	72.7	98.4% (1-10 layers)	Up-scaled DEE

4. Supporting data for the mechanism analyses of DEE

(1) Experimental data

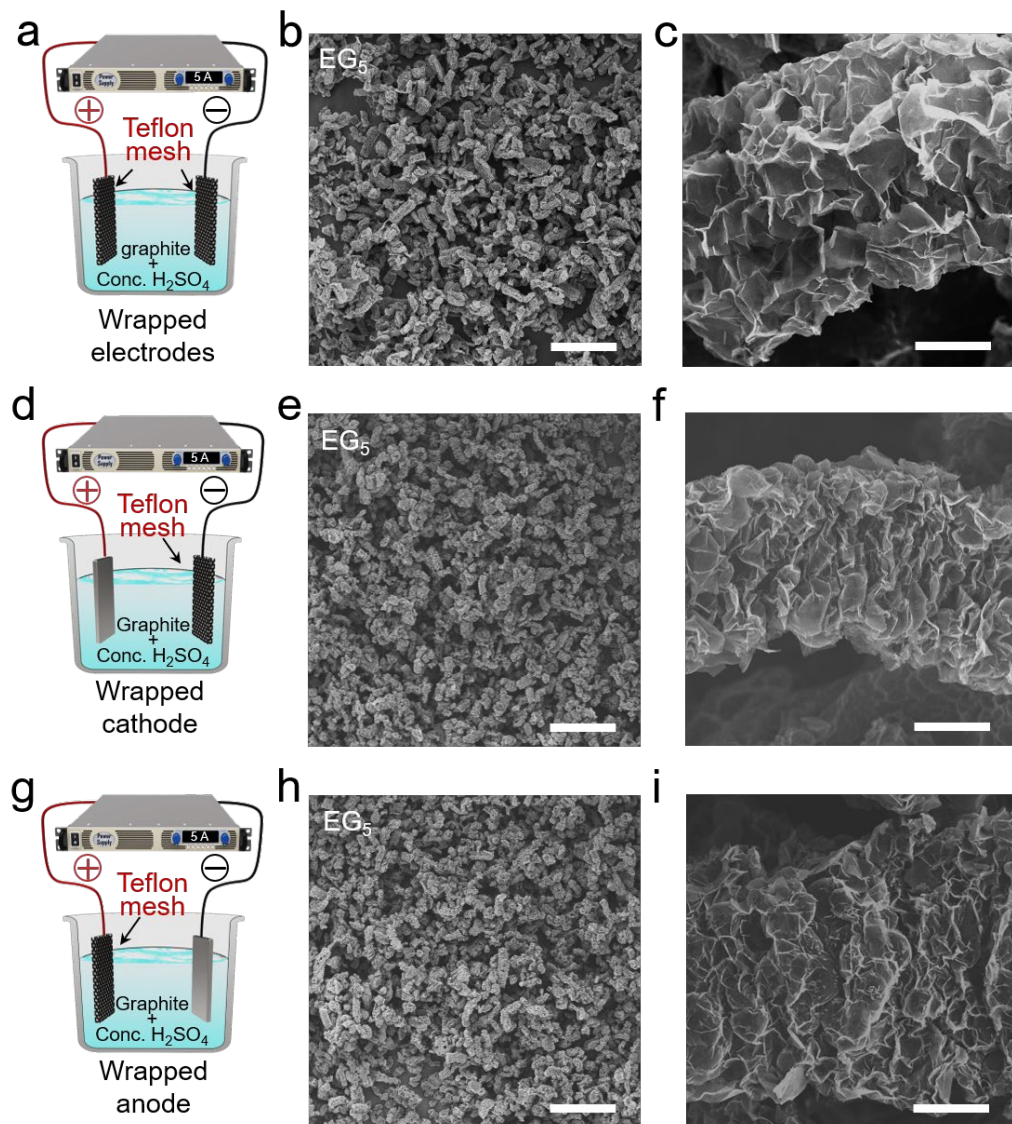


Figure S13. Electrochemical treatments with electrode wrapping. (a–c) Schematic illustration of wrapping both two electrodes (a), the corresponding low-magnification (b), and high-magnification (c) SEM images of EG₅ powder. (Scale bar in b: 400 μ m and c: 20 μ m) (d–f) Schematic illustration of wrapping cathode (d), the corresponding low-magnification (e), and high-magnification (f) SEM images of EG₅ powder. (Scale bar in e: 400 μ m and f: 20 μ m) (g–i) Schematic illustration of wrapping anode (g), the corresponding low-magnification (h), and high-magnification (i) SEM images of EG₅ powder. (Scale bar in h: 400 μ m and i: 20 μ m)

The morphology of the resulting EG powders indicates that wrapping anyone or both two electrode(s) does not inhibit the graphite exfoliation. EG₅ fabricated when wrapping one or two electrode(s) showed a similar morphology with the product in the unwrapping case (Figure S15b, c, e, f, h and i). Therefore, we conclude that graphite exfoliation in the bulk-phase is independent of the intermittent graphite-electrodes contact and is most likely to be caused by the electrolysis products.

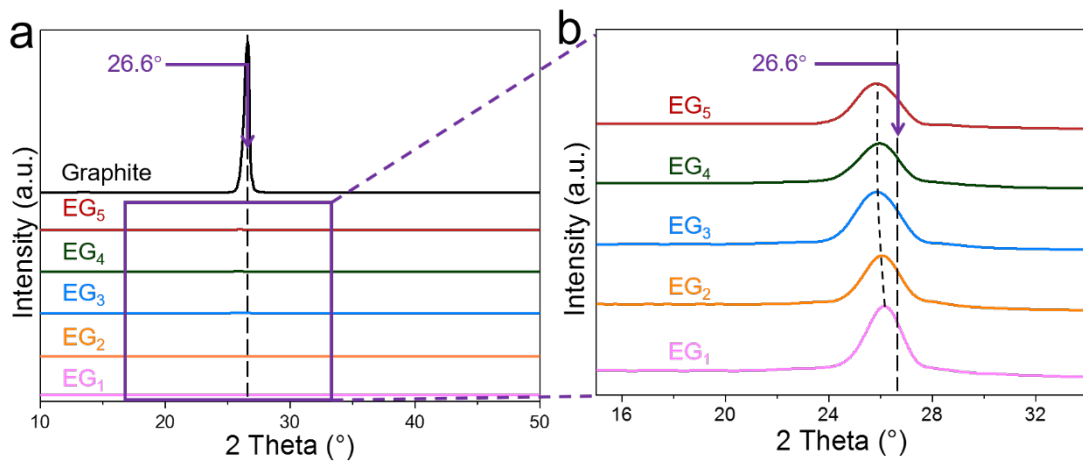


Figure S14. Structure evolution of the graphite during DEE. (a) XRD patterns of graphite, EG₁, EG₂, EG₃, EG₄ and EG₅. (b) The magnified area in Figure S13a.

The resulting expanded graphite products are termed as EG_x, where x represents the duration of electrochemical treatment. Apart from the increasing FWHM as presented in the main text, the (002) reflection peaks in XRD patterns of the intermediate products during DEE showed significant blue shift (Figure S13a and b) from 26.6° (graphite precursor) to 25.8° (EG₅). These data also indicate the structure disordering in the (002) direction as a result of increased interlayer spacing and graphite exfoliation during DEE.²⁰

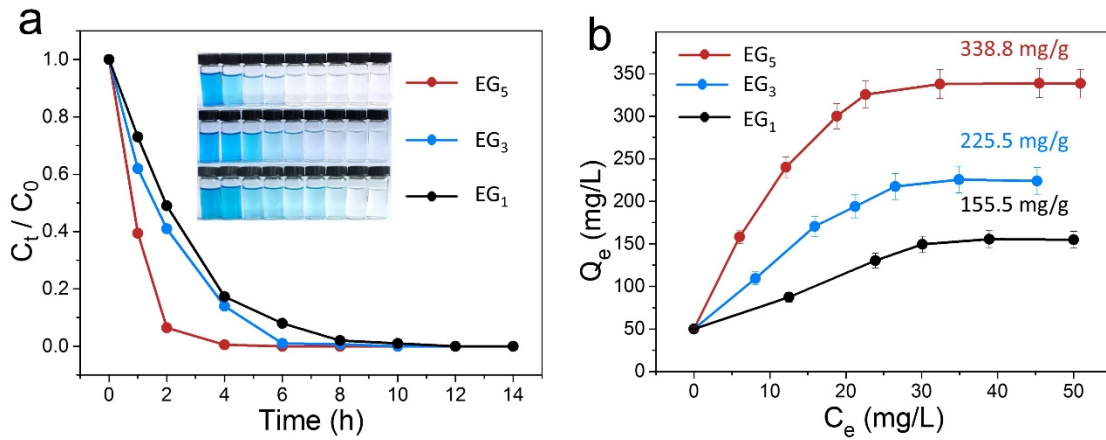


Figure S15. Expansion process of the graphite during DEE. (a) Adsorption kinetic curves of EG₁, EG₃ and EG₅. (b) Adsorption isotherm curves of EG₁, EG₃, and EG₅.

The volume expansion during DEE is obvious and changes over time during DEE. To quantitatively probe the exfoliation process, we measured the MB adsorption kinetic curves and adsorption isotherm curve (Langmuir adsorption model is employed here),^{15,36,37} based on which the absorption rate, absorption capacity and MB-SSA of EG_x can be confirmed (Note S3). As presented in Figure S14a, the absorption rate increases gradually from 0.017 mg/h for EG₁ to 0.025 mg/h for EG₃ and to 0.05 mg/h for EG₅. Absorption capacity and MB-SSA shows a similar change trend. EG₁ and EG₃ have an absorption capacity of 155.5 mg/g and 225.5 mg/g, which corresponds to an MB-SSA of 380.6 m²/g and 552.1 m²/g, respectively. For EG₅, the absorption capacity increased to 338.8 mg/g, which corresponds to an MB-SSA of 829.4 m²/g (Figure S14b).

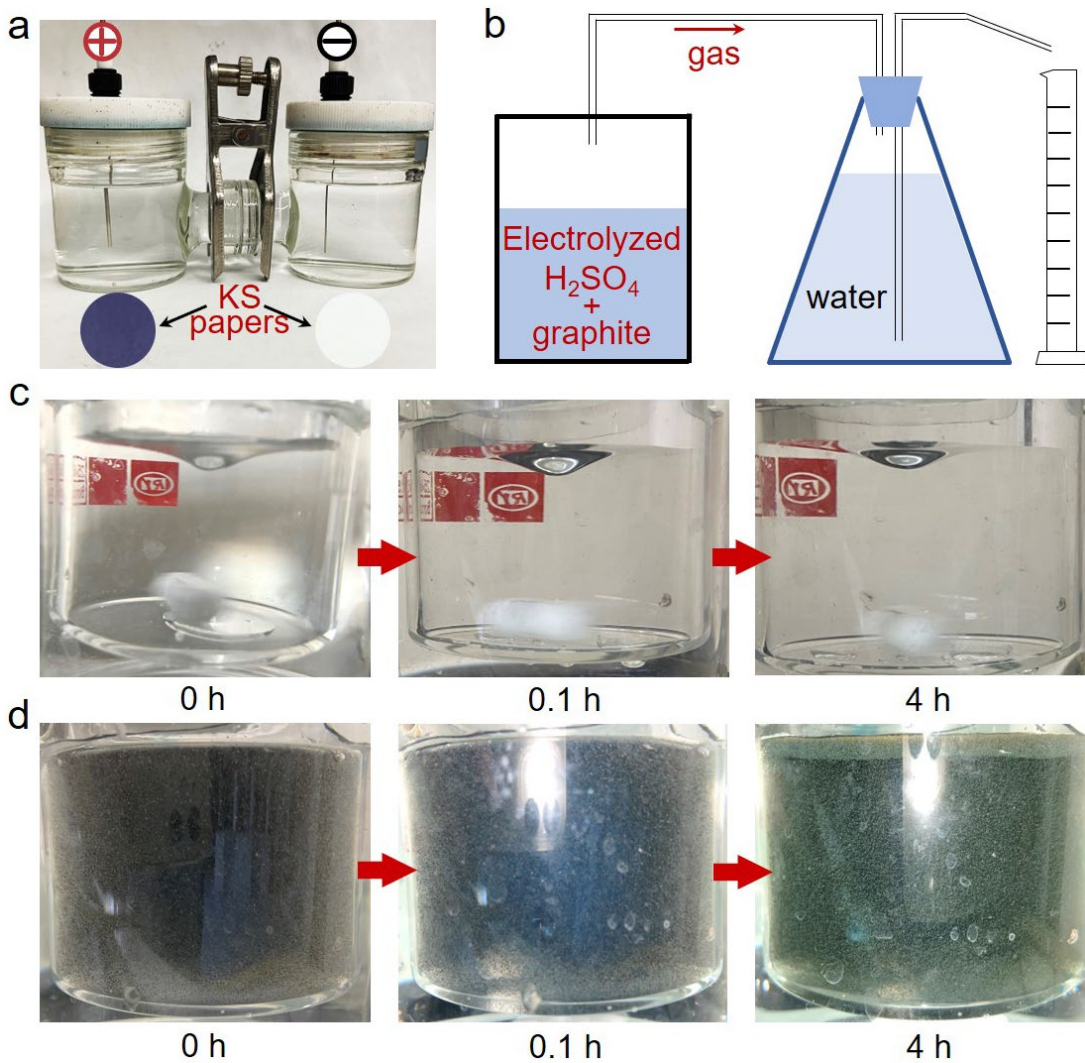


Figure S16. Properties of the electrolyzed H_2SO_4 . (a) Setup of two-electrode system with separated electrodes to collect the electrolysis products forming near individual electrode after DC (5 A) application for 5 h. KS paper turned blue upon exposure to the electrolyte near the anode whereas no color change was observed for KS paper treated by the electrolyte near the cathode. (b) Schematic illustration of the setup for gas collection. (c, d) Photographs show the state of the electrolyzed H_2SO_4 during the gas collection before (c) and after (d) introduction of graphite flakes.

The electrolyzed H_2SO_4 does not produce obvious bubbles in the solution at room temperature even after up to 24 h of stirring. However, upon graphite introduction, many bubbles generated and the graphite flakes gradually expanded afterwards, which is similar to the phenomenon observed during DEE. This similarity validated the electrolyzed H_2SO_4 , rather than the intermittent graphite-electrodes contact, should be responsible for the exfoliation of dispersing graphite during DEE.

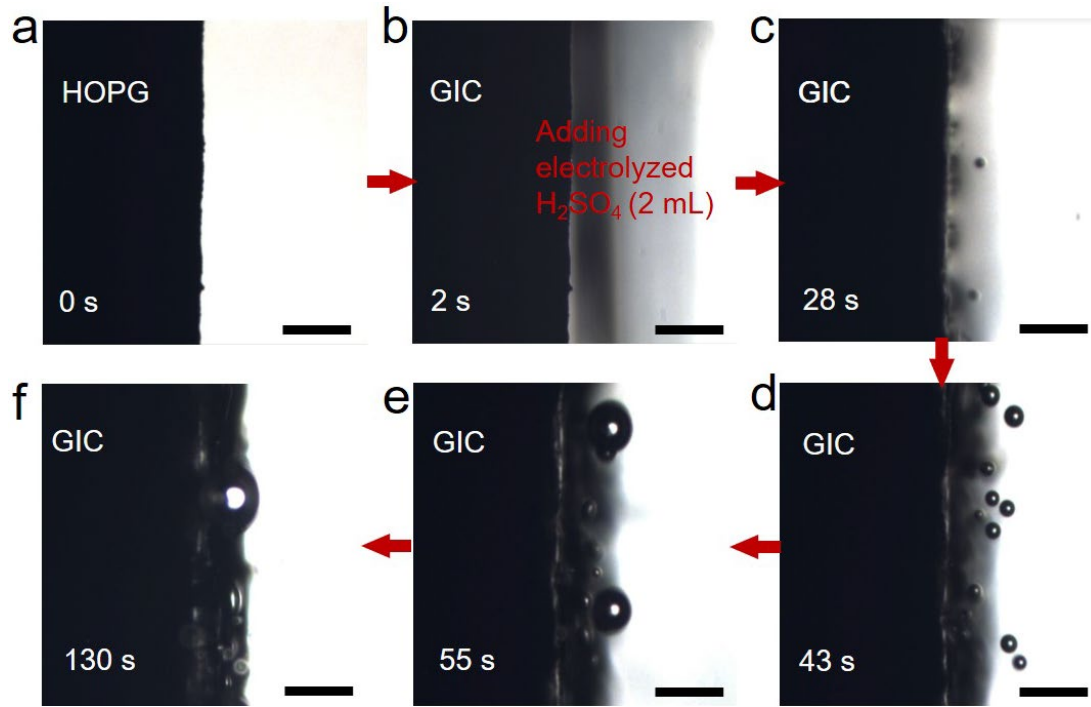


Figure S17. Bubbles appear at the interface of GIC and the electrolyzed H₂SO₄. (a) OM image of HOPG. (b–f) OM images captured at different times showing the HOPG immersed in the Electrolyzed H₂SO₄ and the bubbles appear at the interface of GIC and electrolyzed H₂SO₄. (Scale bars in a–f: 200 μ m)

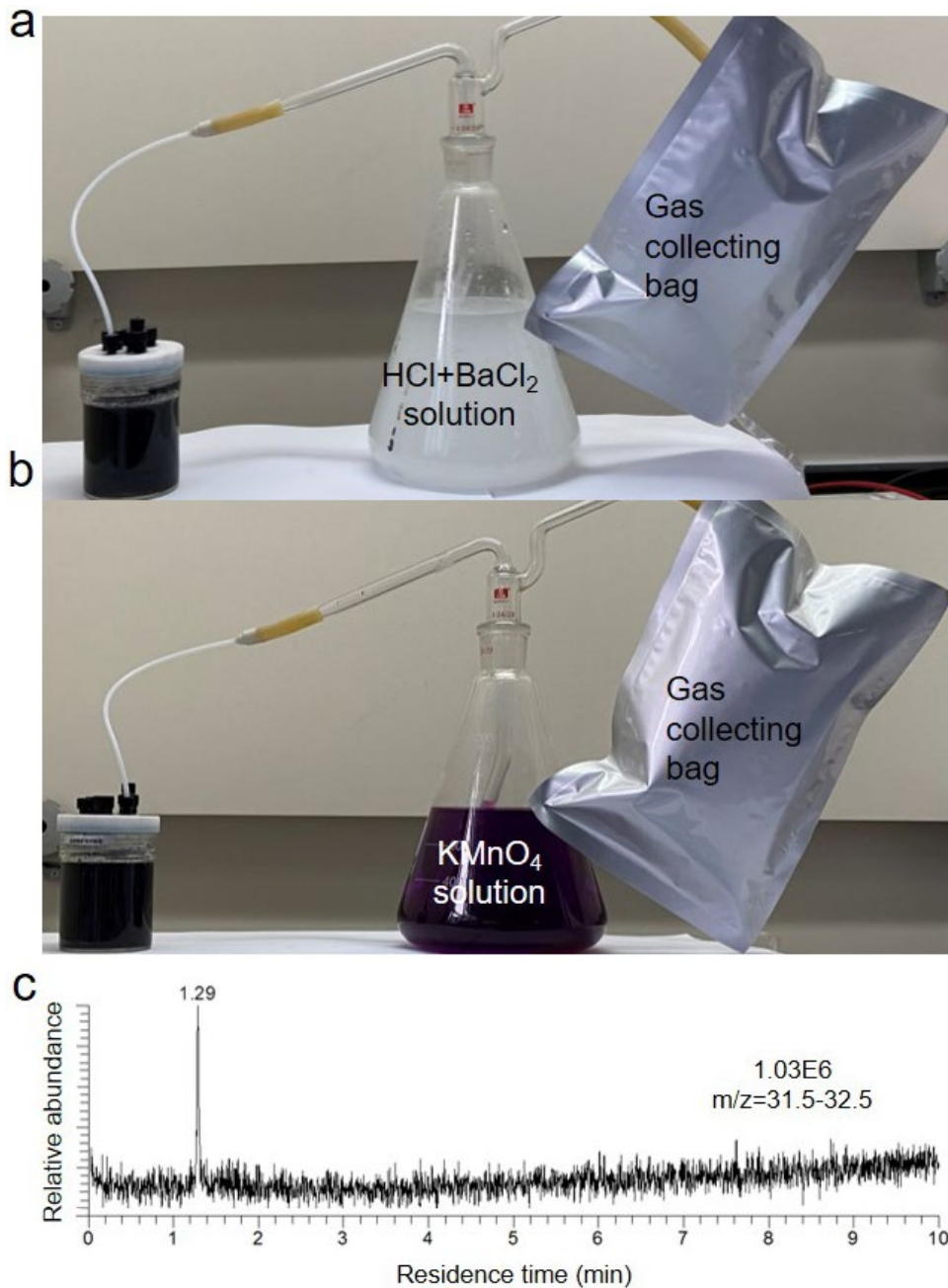


Figure S18. Analyses of the gas generated during the DEE. (a, b) The collection and analysis of the gas generating during the DEE by passing the gas through aqua solution of BaCl₂ (with HCl) and KMnO₄, respectively. (c) The GC-MS signal of the collected exhaust after passing through the BaCl₂ (with HCl) solution.

White precipitate appears when the exhaust is introduced into the mixture solution of HCl and BaCl₂ (Figure s17a) whereas no color change was observed when the exhaust is introduced into the KMnO₄ solution (Figure s17b). These observations suggest the formation of SO₃ during the DEE. The gas after passing through the BaCl₂ (with HCl) solution is collected by a bag and was further confirmed to be O₂ by the GC-MS result (Figure s17c), which determines the generation of O₂ and SO₃ as the gaseous products of the DEE.

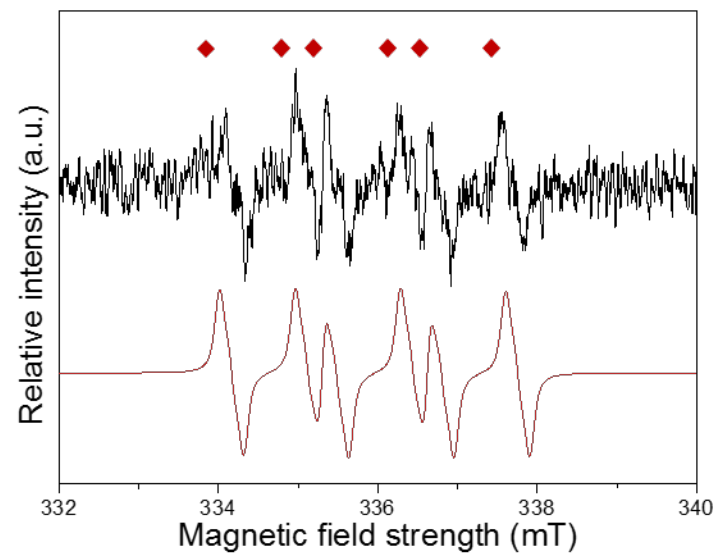


Figure S19. ESR analysis of radical in electrolyzed H₂SO₄. The ESR spectrum (black) and the simulated spectrum (red) of the electrolyzed H₂SO₄. (♦: DMPO-SO₄), [Temp]=25 °C, [Electrolyzed H₂SO₄]= 4 mM, [DMPO]=50 mM.

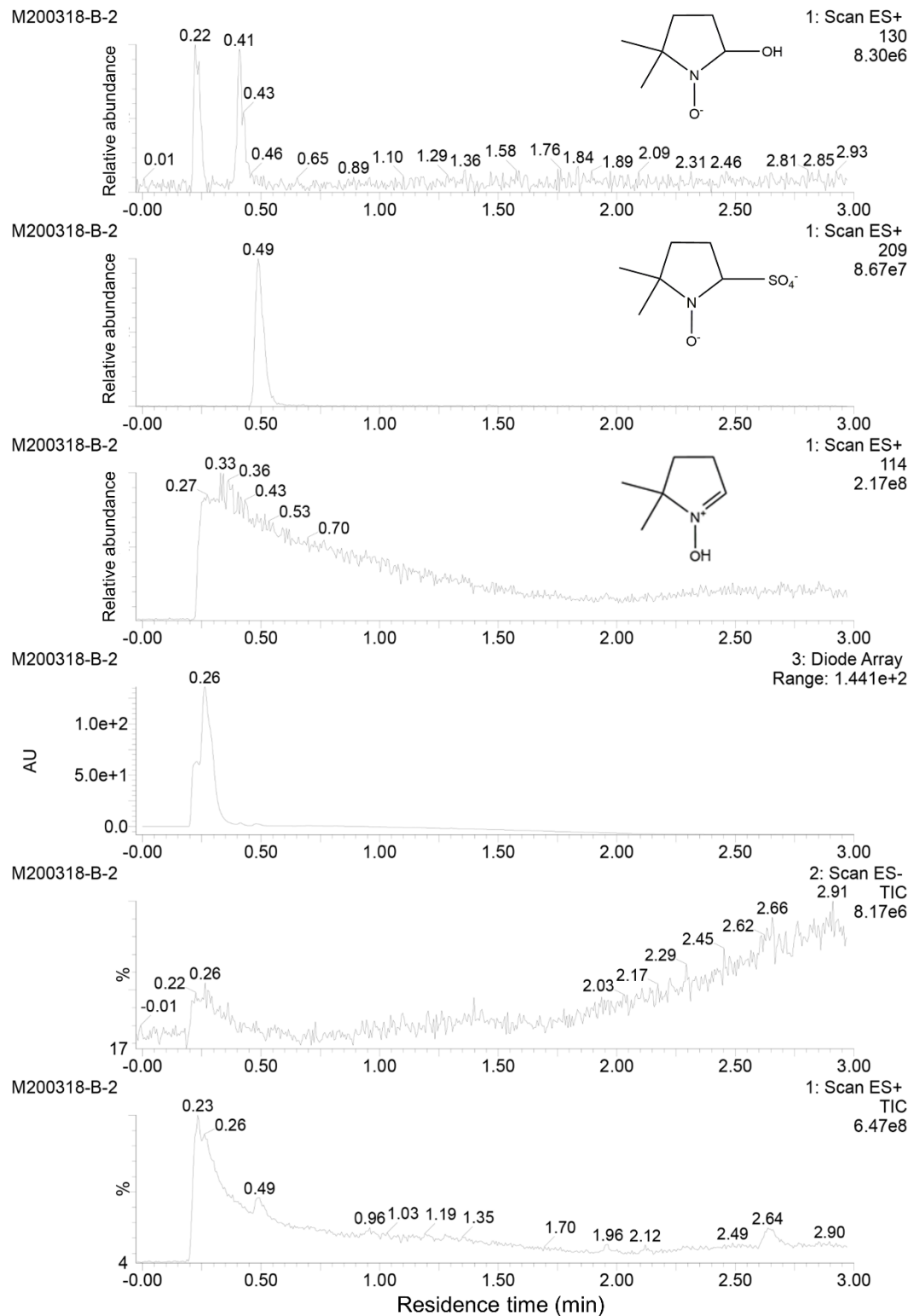
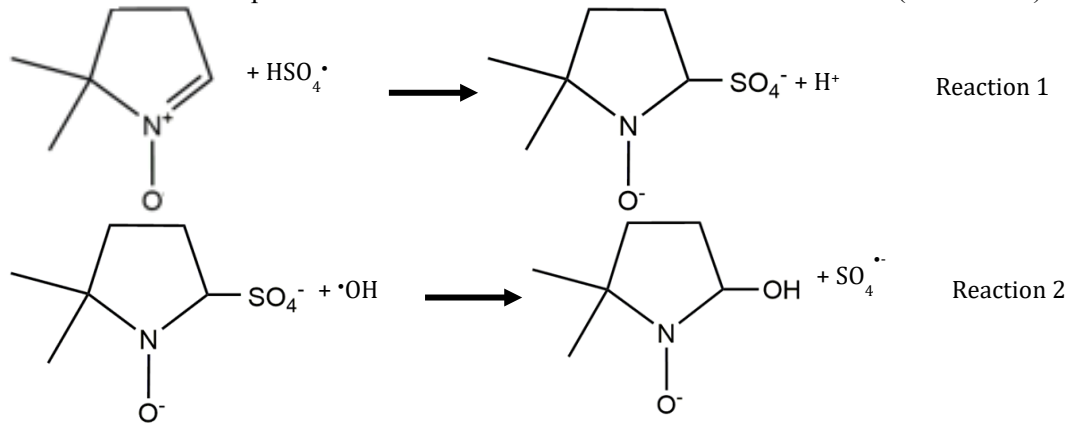


Figure S20. LC-MS analysis of radical in electrolyzed H₂SO₄. The high-performance liquid chromatography-high resolution mass spectra (LC-MS) results of the electrolyzed H₂SO₄.

Electron spin resonance (ESR) spectra and high-performance liquid chromatography-high resolution mass spectra (LC-MS) were used to validate the formation of HSO_4^\cdot . DMPO- SO_4 has been identified in the mixture of the electrolyzed H_2SO_4 and DMPO by hyperfine splitting constant ($\text{AN}=1.32$, $\text{AH}=0.95$, $\text{A}_{\gamma_1}\text{H}=0.14$, $\text{A}_{\gamma_2}\text{H}=0.08$) in Figure S19.³⁸ This can be explained by the radical adduct reaction between DMPO and HSO_4^\cdot in the H_2SO_4 (Reaction 1). The signals of $\text{M/Z}=114$, 130 and 209 in the LC-MS spectra of the mixture of DMPO and electrolyzed H_2SO_4 (Figure S20) can be ascribed to the protonated DMPO, DMPO-OH and DMPO- SO_4 , respectively, indicating the presence of HSO_4^\cdot in the electrolyzed H_2SO_4 . DMPO-OH in the LC-MS spectra may result from the nucleophilic substitution reaction between $\cdot\text{OH}$ and DMPO- SO_4 (Reaction 2).³⁹



(2) Calculation details

All the density functional theory (DFT) calculations were conducted using the Vienna Ab initio Simulation Package (VASP). The Perdew-Burke-Ernzerhof (PBE) functional was used with the plane-wave cut-off energy of 400 eV. All the gas molecules were calculated in a unit cell of $20\times 20\times 20 \text{ \AA}^3$ and the distance between the graphite layers was set to 4 \AA as determined experimentally for stage 1 GIC to describe the effect from graphite layer during the interlayer reactions. Structural optimizations were conducted with the convergence force smaller than 0.05 eV \AA^{-1} . All the transition states were searched using the climbing image nudged elastic band (NEB) method the convergence force smaller than 0.05 eV \AA^{-1} . Free energy corrections were applied in this work at the temperature of 298 K acting on all the energetic results. All the transitional, rotational and vibrational motions were considered in the free energy correction and the calculations were conducted using Gaussian software. Zero-point energy (ΔZPE), inner energy (ΔU), entropy part ($-\text{T}\Delta\text{S}$) and total energy change (ΔE) were put together to give the reaction free energy change (ΔG), which could be written as (Equation 1 (Eq. 1)):

$$\Delta\text{G}=\Delta\text{E}+\Delta\text{ZPE}+\Delta\text{U}-\text{T}\Delta\text{S} \quad (\text{Eq. 1})$$

The energy evolution of $\text{H}_2\text{S}_2\text{O}_8$ cleavage.

Three pathways are possible for the $\text{H}_2\text{S}_2\text{O}_8$ cleavage including two heterolysis cleavages and one homolytic cleavage (P1, P2 and P3, as presented in Table S4). DFT calculations reveal the change of free energy (ΔG) and energy barrier (G_a) of every primitive reaction in each pathway. As shown in Table S4, the first step of P1 and P2 have much higher ΔG (1.23 eV and 6.31 eV, respectively) than P3 (-0.43 eV). Also, P3 has the smallest G_a (P1: 2.22 eV; P2: 6.31 eV and P3: 0.78 eV) among the three cleavage pathways at room temperature. Hence, homolytic cleavage is the most promising pathway.

Table S4. Computed ΔG and G_a of the $\text{H}_2\text{S}_2\text{O}_8$ cleavage.

Pathway	Reaction	ΔG (eV)	G_a (eV)
P1: heterolysis cleavage	$\text{H}_2\text{S}_2\text{O}_8 \rightarrow \text{HSO}_3^\cdot + \text{HSO}_5^\cdot$	1.23	2.22
	$\text{HSO}_3^\cdot \rightarrow \text{SO}_3 + \text{H}^\cdot$	3.71	-
	$\text{HSO}_5^\cdot + \text{H}^\cdot \rightarrow \text{H}_2\text{SO}_5$	-2.38	-
	$\text{H}_2\text{SO}_5 \rightarrow \text{HSO}_4^\cdot + \cdot\text{OH}$	1.00	-
	$\text{HSO}_4^\cdot \rightarrow \text{SO}_3 + \cdot\text{OH}$	1.20	1.76

	$2\cdot\text{OH} \rightarrow \text{H}_2\text{O}+\text{O}^\cdot$	-0.49	0.28
	$2\text{O}^\cdot \rightarrow \text{O}_2$	-5.74	0.17
P2: heterolysis cleavage	$\text{H}_2\text{S}_2\text{O}_8 \rightarrow \text{HSO}_3^+ + \text{HSO}_5^-$	6.31	6.31
	$\text{HSO}_3^+ \rightarrow \text{SO}_3 + \text{H}^+$	3.18	-
	$\text{HSO}_5^\cdot + \text{H}^+ \rightarrow \text{H}_2\text{SO}_5$	-1.23	-
	$\text{H}_2\text{SO}_5 \rightarrow \text{HSO}_4^\cdot + \cdot\text{OH}$	1.00	-
	$\text{HSO}_4^\cdot \rightarrow \text{SO}_3 + \cdot\text{OH}$	1.20	1.76
	$2\cdot\text{OH} \rightarrow \text{H}_2\text{O}+\text{O}^\cdot$	-0.49	0.28
	$2\text{O}^\cdot \rightarrow \text{O}_2$	-5.74	0.17
P3: homolytic cleavage	$\text{H}_2\text{S}_2\text{O}_8 \rightarrow 2\text{HSO}_4^\cdot$	-0.43	0.78

Table S5. Computed ΔG and G_a of HSO_4^\cdot disproportionation in bulk electrolyte and in the graphite galleries.

Reaction site	Reaction	ΔG (eV)	G_a (eV)
in bulk electrolyte	$\text{HSO}_4^\cdot \rightarrow \text{SO}_3 + \cdot\text{OH}$	1.20	1.76
	$2\cdot\text{OH} \rightarrow \text{H}_2\text{O}+\text{O}^\cdot$	-0.49	0.28
	$2\text{O}^\cdot \rightarrow \text{O}_2$	-5.74	0.17
in graphite galleries	$\text{HSO}_4^\cdot + \text{GIC}-\text{HSO}_4^- \rightarrow \text{GIC}-\text{HSO}_4^\cdot + \text{HSO}_4^-$	-6.64	0.00
	$\text{GIC}-\text{HSO}_4^\cdot \rightarrow \text{GIC}-\text{SO}_3 + \text{GIC}-\cdot\text{OH}$	-1.17	0.91
	$2\text{GIC}-\cdot\text{OH} \rightarrow \text{GIC}-\text{H}_2\text{O} + \text{GIC}-\text{O}^\cdot$	0.10	0.37
	$2\text{GIC}-\text{O}^\cdot \rightarrow \text{GIC}-\text{O}_2$	-4.77	0.17

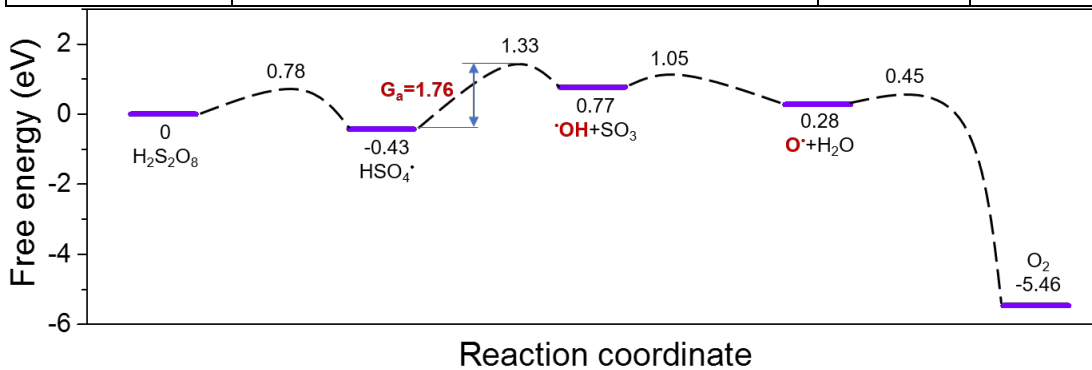


Figure S21. The energy profile of $\text{H}_2\text{S}_2\text{O}_8$ homolytic cleavage and HSO_4^\cdot disproportionation in the bulk-phase electrolyte.

For the homolytic cleavage pathway, the cleavage product is HSO_4^\cdot , whose presence in the bulk electrolyte has been confirmed by the experimental results. The formation of HSO_4^\cdot inside the graphite layered structure is also possible since the electron transfer between the intercalated HSO_4^- and the electronically oxidized graphite layers (electron poor) require no extra energy input. Therefore, disproportionation of the generated HSO_4^\cdot into O_2 and SO_3 can occur possibly in the bulk electrolyte and inside graphite structure. We calculate the related energy

changes and reaction barriers (Table S4). The results show that disproportionation inside the graphite layers is more dynamically favorable because of a smaller energy barrier (only about 50% of that in the bulk electrolyte).

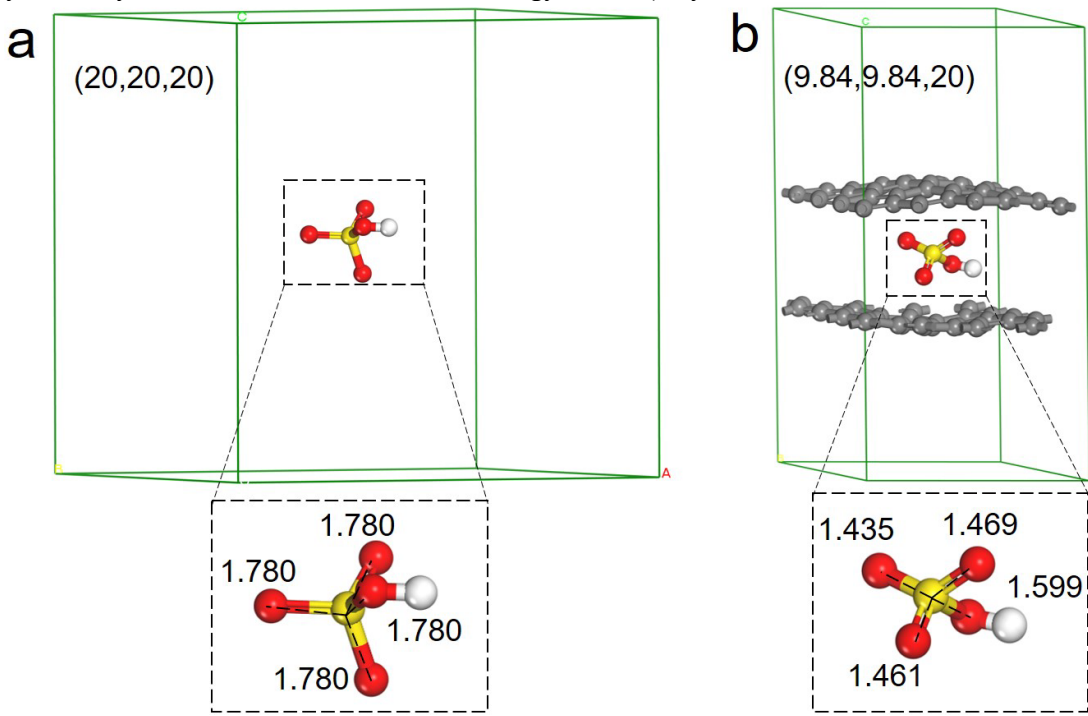


Figure S22. The optimized molecular configurations of HSO_4^\bullet in bulk electrolyte and in the graphite galleries. (a) The S-O bond length of HSO_4^\bullet in the bulk electrolyte is 1.780 Å. (b) The S-O bond length of HSO_4^\bullet in graphite galleries are 1.435, 1.461, 1.469 and 1.599 Å.

The HSO_4^\bullet has shorter S-O bonds length in the graphite galleries (1.78 Å for HSO_4^\bullet in bulk liquid; 1.435, 1.461, 1.469 and 1.599 Å for HSO_4^\bullet in graphite galleries) because of the confinement of graphene layers. This is also reflected in the configuration and lattice of HSO_4^\bullet (the lattice constant of HSO_4^\bullet changes from (20,20,20) for HSO_4^\bullet in the bulk liquid to (9.84,9.84,20) for HSO_4^\bullet in the graphite galleries) (Figure S22a and b). Also, it is calculated that the HSO_4^\bullet in the graphite galleries has higher chemical potential than that in the bulk liquid (3.13 eV relative to the HSO_4^\bullet in bulk-phase). This difference in chemical potential should be responsible for the significantly decreased energy barrier of HSO_4^\bullet disproportionation inside the graphite structure.

5. Supporting data for fabrication and characterizations of DEE-graphene based films and strain sensors.

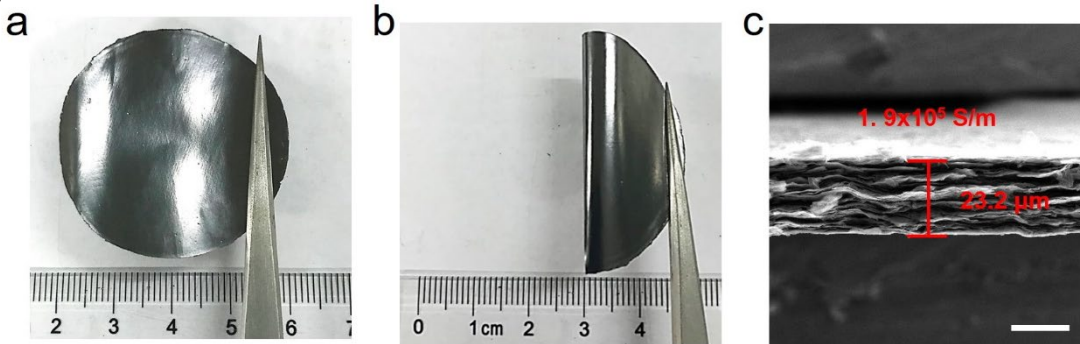


Figure S23. Morphology of DEE-graphene based film. Photographs (a, b) and side-view SEM image (c) of the graphene film. (Scale bar in c: 20 μm)

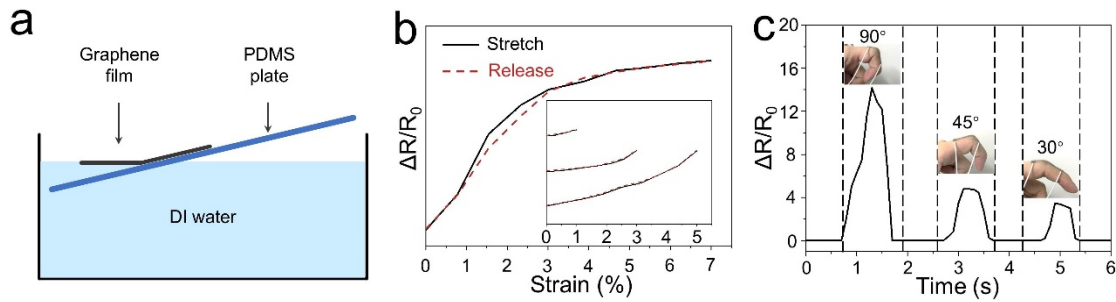


Figure S24. Fabrication and performance of strain sensor. (a) Illustration for the preparation of DEE-graphene based sensors. (b) The stretch and release behavior of the sensor. (c) Using the sensor to monitor the real-time finger bending states.

Table S6. Detection limit, cycling stability and response time of graphene-base sensors in different works.

LPEG: liquid-phase exfoliation graphene

Material	Detection limit	Cycling stability	Response time (ms)	Ref.
CVD-G	0.2% strain	NA	NA	40
rGO	NA	1000 cycles	20	41
LPEG	NA	4000 cycles	NA	42
LPEG	0.03% strain	>8 h	NA	43
CVD-G	0.015% strain	NA	NA	44
GO	NA	NA	NA	45
EEG	NA	NA	NA	1
LIG	1%	20000 cycles	NA	46
LPEG	NA	NA	NA	47
LPEG	NA	1000 cycles	NA	48
CVD-G	0.105% strain	NA	NA	49
CVD-G	NA	NA	NA	50
rGO	<0.1% strain	5000 cycles	NA	51
GN	NA	400 cycles	NA	52
rGO	0.2% strain	10000 cycles	<100	53
CVD-G	NA	1000 cycles	72	54
DEE-graphene	0.05% strain	>8600 cycles	<100	Our work

GN: graphene nanoplatelets

6. Supporting notes

Note S1. Raman analyses of the graphite precursor and DEE-graphene.

Raman spectra were used to assess the structural integrity and defect density of precursor graphite and graphene. It is well established that the crystal quality parameters including the crystalline domain size (L_a), the distance between defects (L_D) and the density of defects (n_D) can be deduced from Raman spectra of graphite and graphene. L_a (Eq. 2):⁵⁵

$$L_a = (2.4 \times 10^{-10}) \times \lambda^4 \times \left(\frac{I_D}{I_G}\right)^{-1} \quad (\text{Eq. 2})$$

where λ (nm) is the wavelength of the Raman laser.

The L_D can be evaluated from Raman I_D/I_G value using (Eq. 3):

$$\frac{I_D}{I_G} = C_A \frac{(r_A^2 - r_S^2)}{(r_A^2 - 2r_S^2)} \left[e^{-\frac{\pi r_S^2}{L_D^2}} - e^{-\frac{\pi(r_A^2 - 2r_S^2)}{L_D^2}} \right] \quad (\text{Eq. 3})$$

where r_S (1 nm) and r_A (3.1 nm) are the radii of the ‘structurally disordered’ area and the ‘activated’ area around the ion-induced defects, respectively.⁵⁶ The factor C_A (4.2) is defined by the electron–phonon matrix elements.⁵⁷ n_D can be evaluated by (Eq. 4):⁴

$$n_D = 10^{14} / \pi L_D^2 \quad (\text{Eq. 4})$$

Note S2. Recycling of H_2SO_4 .

After the DEE process, a filter (300 mesh for 300 mesh graphite precursor) was used to separate the residual H_2SO_4 and the exfoliated product. Because H_2SO_4 was the only electrolyte and no impurity was introduced, the filtered H_2SO_4 could be recycled for the next round of fabrication.

Note S3. The MB absorption measurement of the exfoliated products.

The EG_1 , EG_3 , and EG_5 after water washing were directly used for the tests without drying. 4 mg EG_1 , EG_3 , and EG_5 were respectively added to 20 mL methylene blue aqueous solution (10 mg/L) and stirred for 24 h to ensure getting the absorption equilibrium. Afterwards, the solution was centrifuged at 8000 rpm to remove the exfoliated products in the solution and a 2 mL supernatant solution was obtained for UV-Vis spectroscopy analyses to monitor the absorption process.

The adsorption isotherms were obtained by changing the initial MB concentrations. The absorption amounts (Q_e) and the maximum adsorption capacity (Q_m) of methylene blue in EG_1 , EG_3 , and EG_5 were assessed by the following equation. Q_e (Eq. 5):⁵⁸

$$Q_e = (C_0 - C_e)V/m \quad (\text{Eq. 5})$$

Herein, Q_e (mg/g) is the absorption amount of methylene blue at absorption equilibrium, C_0 (mg/L) is the initial concentration of methylene blue solution, C_e (mg/L) is the concentration of methylene blue when reaching the absorption equilibrium state, V (20 mL) is the volume of methylene blue used in each experience and m (4 mg) is the mass of EG powder. Q_m (Eq. 6):³⁶

$$Q_e = Q_m b C_e / (1 + C_e) \quad (\text{Eq. 6})$$

where b represents the equilibrium constant (in L mg/g).

Note S4. The KS paper test of the electrolyzed H_2SO_4 .

Firstly, 0.5 mL samples (electrolyzed H_2SO_4 after different time of electrochemistry treatment) taking out from the bulk electrolyte were respectively and slowly added to 10 mL DI water. Then the KS papers were respectively immersed into the above diluted solutions for 5 s. Afterwards, the papers were taken out for color observation.

Note S5. The extraction and analysis of electrolysis products of H_2SO_4 .

Firstly, the electrolyzed H_2SO_4 was added into the NaOH solution (200 mL, 0.05g/mL) dropwise in a water bath at 5 °C until the solution approaches neutral (pH ~7). Then, the rotary evaporator was used to remove the water (at 40°C and 0.06 MPa) from the solution and extract the solid product. Finally, the obtained white solid was ground (>200 mesh) and then characterized using XRD to get the structure information.

Note S6. The gas collection experiment.

100 mL electrolyzed H_2SO_4 was transferred into the beaker as schematically illustrated in Figure S18b-d. A magnetic stirring apparatus (300 r/min) and cooling water circulation machine were used to keep the temperature of the mixture at 25 °C. We get the volume of the insoluble gas generated from the reaction mixture by recording

the volumes of the drained water at different times. Under the same conditions, 100 mg graphite flakes were added into the electrolyzed H_2SO_4 and the volumes of the drained water at different times were recorded for comparison.

Note S7. The LC-MS analysis of the electrolyzed H_2SO_4 .

1.0 μL electrolyzed H_2SO_4 was dissolved into 1.0 mL DMSO. 1.0 mL 5.0 mM DMPO in DMSO was added into the above solution and reacted for 1 min at room temperature. The obtained mixture was neutralized by NH_4OH and then used for LC-MS analysis.

Note S8. Fabrication of the graphene films.

Firstly, a gel film was prepared by vacuum filtrating 50 mL DEE-graphene dispersion in DMF (0.1 mg/mL) onto a porous alumina membrane. Then, the gel film was dried in an oven at 50 $^{\circ}\text{C}$ for 24 h. Then, the dried film was peeled off from the alumina membrane and put into a piston-cylinder apparatus for pressing (20 MPa, 2 min). A compact and free-standing film can be obtained after pressure relief and demolding (Figure S23a, b and c).

7. References

- (1) Li, X.; Yang, T.; Yang, Y.; Zhu, J.; Li, L.; Alam, F. E.; Li, X.; Wang, K.; Cheng, H.; Lin, C. Te; et al. Large-Area Ultrathin Graphene Films by Single-Step Marangoni Self-Assembly for Highly Sensitive Strain Sensing Application. *Adv. Funct. Mater.* **2016**, *26* (9), 1322–1329.
- (2) Hernandez, Y.; Nicolosi, V.; Lotya, M.; Blighe, F. M.; Sun, Z.; De, S.; McGovern, I. T.; Holland, B.; Byrne, M.; Gun’ko, Y. K.; et al. High-Yield Production of Graphene by Liquid-Phase Exfoliation of Graphite. *Nat. Nanotechnol.* **2008**, *3* (9), 563–568.
- (3) Cheng, Z.; Zhou, Q.; Wang, C.; Li, Q.; Wang, C.; Fang, Y. Toward Intrinsic Graphene Surfaces: A Systematic Study on Thermal Annealing and Wet-Chemical Treatment of SiO₂-Supported Graphene Devices. *Nano Lett.* **2011**, *11* (2), 767–771.
- (4) Cançado, L. G.; Jorio, A.; Ferreira, E. H. M.; Stavale, F.; Achete, C. A.; Capaz, R. B.; Moutinho, M. V. O.; Lombardo, A.; Kulmala, T. S.; Ferrari, A. C. Quantifying Defects in Graphene via Raman Spectroscopy at Different Excitation Energies. *Nano Lett.* **2011**, *11* (8), 3190–3196.
- (5) Grodecki, K.; Jozwik, I.; Baranowski, J. M.; Teklinska, D.; Strupinski, W. SEM and Raman Analysis of Graphene on SiC(0001). *Micron.* **2016**, *80* (2), 20–23.
- (6) Wang, G.; Zhang, M.; Zhu, Y.; Ding, G.; Jiang, D.; Guo, Q.; Liu, S.; Xie, X.; Chu, P. K.; Di, Z.; et al. Direct Growth of Graphene Film on Germanium Substrate. *Sci. Rep.* **2013**, *3*, 1–6.
- (7) Hummers, W. S.; Offeman, R. E. Preparation of Graphitic Oxide. *J. Am. Chem. Soc.* **1958**, *80* (6), 1339.
- (8) Pei, S.; Zhao, J.; Du, J.; Ren, W.; Cheng, H. M. Direct Reduction of Graphene Oxide Films into Highly Conductive and Flexible Graphene Films by Hydrohalic Acids. *Carbon.* **2010**, *48* (15), 4466–4474.
- (9) Green, A. A.; Hersam, M. C. Solution Phase Production of Graphene with Controlled Thickness via Density Differentiation. *Nano Lett.* **2009**, *9* (12), 4031–4036.
- (10) Lin, T.; Chen, J.; Bi, H.; Wan, D.; Huang, F.; Xie, X.; Jiang, M. Facile and Economical Exfoliation of Graphite for Mass Production of High-Quality Graphene Sheets. *J. Mater. Chem. A.* **2013**, *1* (3), 500–504.
- (11) Knieke, C.; Berger, A.; Voigt, M.; Klupp Taylor, R. N.; Röhrl, J.; Peukert, W. Scalable Production of Graphene Sheets by Mechanical Delamination. *Carbon.* **2010**, *48* (11), 3196–3204.
- (12) Arao, Y.; Mizuno, Y.; Araki, K.; Kubouchi, M. Mass Production of High-Aspect-Ratio Few-Layer-Graphene by High-Speed Laminar Flow. *Carbon.* **2016**, *102*, 330–338.
- (13) Paton, K. R.; Varrla, E.; Backes, C.; Smith, R. J.; Khan, U.; O’Neill, A.; Boland, C.; Lotya, M.; Istrate, O. M.; King, P.; et al. Scalable Production of Large Quantities of Defect-Free Few-Layer Graphene by Shear Exfoliation in Liquids. *Nat. Mater.* **2014**, *13* (6), 624–630.
- (14) Chen, J.; Shi, W.; Fang, D.; Wang, T.; Huang, J.; Li, Q.; Jiang, M.; Liu, L.; Li, Q.; Dong, L.; et al. A Binary Solvent System for Improved Liquid Phase Exfoliation of Pristine Graphene Materials. *Carbon.* **2015**, *94*, 405–411.
- (15) Lin, S.; Dong, L.; Zhang, J.; Lu, H. Room-Temperature Intercalation and ~1000-Fold Chemical Expansion for Scalable Preparation of High-Quality Graphene. *Chem. Mater.* **2016**, *28* (7), 2138–2146.
- (16) Geng, X.; Guo, Y.; Li, D.; Li, W.; Zhu, C.; Wei, X.; Chen, M.; Gao, S.; Qiu, S.; Gong, Y.; et al. Interlayer Catalytic Exfoliation Realizing Scalable Production of Large-Size Pristine Few-Layer Graphene. *Sci. Rep.* **2013**, *3*, 1–12.
- (17) He, P.; Gu, H.; Wang, G.; Yang, S.; Ding, G.; Liu, Z.; Xie, X. Kinetically Enhanced Bubble-Exfoliation of Graphite toward High-Yield Preparation of High-Quality Graphene. *Chem. Mater.* **2017**, *29* (20), 8578–8582.
- (18) Dimiev, A. M.; Ceriotti, G.; Metzger, A.; Kim, N. D.; Tour, J. M. Chemical Mass Production of Graphene Nanoplatelets in ~100% Yield. *ACS Nano.* **2016**, *10* (1), 274–279.
- (19) La, M. D. D.; Bhargava, S.; Bhosale, S. V. Improved and A Simple Approach For Mass Production of Graphene Nanoplatelets Material. *ChemistrySelect.* **2016**, *1* (5), 949–952.
- (20) Matsumoto, M.; Saito, Y.; Park, C.; Fukushima, T.; Aida, T. Ultrahigh-Throughput Exfoliation of Graphite into Pristine “single-Layer” Graphene Using Microwaves and Molecularly Engineered Ionic Liquids. *Nat. Chem.* **2015**, *7* (9), 730–736.
- (21) Liu, M.; Zhang, X.; Wu, W.; Liu, T.; Liu, Y.; Guo, B.; Zhang, R. One-Step Chemical Exfoliation of Graphite to ~100% Few-Layer Graphene with High Quality and Large Size at Ambient Temperature. *Chem. Eng. J.* **2019**, *355* (June 2018), 181–185.
- (22) Park, K. H.; Kim, B. H.; Song, S. H.; Kwon, J.; Kong, B. S.; Kang, K.; Jeon, S. Exfoliation of Non-Oxidized Graphene Flakes for Scalable Conductive Film. *Nano Lett.* **2012**, *12* (6), 2871–2876.

(23) Li, X.; Zhang, G.; Bai, X.; Sun, X.; Wang, X.; Wang, E.; Dai, H. Highly Conducting Graphene Sheets and Langmuir-Blodgett Films. *Nat. Nanotechnol.* **2008**, *3* (9), 538–542.

(24) Vicalis, L. M.; Mack, J. J.; Mayer, O. M.; Hahn, H. T.; Kaner, R. B. Intercalation and Exfoliation Routes to Graphite Nanoplatelets. *J. Mater. Chem.* **2005**, *15* (9), 974–978.

(25) Wang, J.; Manga, K. K.; Bao, Q.; Loh, K. P. High-Yield Synthesis of Few-Layer Graphene Flakes through Electrolyte. *J. Am. Chem. Soc.* **2011**, *133*, 8888–8891.

(26) Yang, S.; Brüller, S.; Wu, Z. S.; Liu, Z.; Parvez, K.; Dong, R.; Richard, F.; Samori, P.; Feng, X.; Müllen, K. Organic Radical-Assisted Electrochemical Exfoliation for the Scalable Production of High-Quality Graphene. *J. Am. Chem. Soc.* **2015**, *137* (43), 13927–13932.

(27) Wang, S.; Li, R.; Müllen, K.; Hinkel, F.; Feng, X.; Hernandez, Y.; Puniredd, S. R.; Parvez, K. Electrochemically Exfoliated Graphene as Solution-Processable, Highly Conductive Electrodes for Organic Electronics. *ACS Nano.* **2013**, *7* (4), 3598–3606.

(28) Parvez, K.; Wu, Z. S.; Li, R.; Liu, X.; Graf, R.; Feng, X.; Müllen, K. Exfoliation of Graphite into Graphene in Aqueous Solutions of Inorganic Salts. *J. Am. Chem. Soc.* **2014**, *136* (16), 6083–6091.

(29) Yang, S.; Ricciardulli, A. G.; Liu, S.; Dong, R.; Lohe, M. R.; Becker, A.; Squillaci, M. A.; Samori, P.; Müllen, K.; Feng, X. Ultrafast Delamination of Graphite into High-Quality Graphene Using Alternating Currents. *Angew. Chemie - Int. Ed.* **2017**, *56* (23), 6669–6675.

(30) Liu, J.; Poh, C. K.; Zhan, D.; Lai, L.; Lim, S. H.; Wang, L.; Liu, X.; Gopal Sahoo, N.; Li, C.; Shen, Z.; et al. Improved Synthesis of Graphene Flakes from the Multiple Electrochemical Exfoliation of Graphite Rod. *Nano Energy* **2013**, *2* (3), 377–386.

(31) Rao, K. S.; Senthilnathan, J.; Cho, H. W.; Wu, J. J.; Yoshimura, M. Soft Processing of Graphene Nanosheets by Glycine-Bisulfate Ionic-Complex-Assisted Electrochemical Exfoliation of Graphite for Reduction Catalysis. *Adv. Funct. Mater.* **2015**, *25* (2), 298–305.

(32) Su, C. Y.; Lu, A. Y.; Xu, Y.; Chen, F. R.; Khlobystov, A. N.; Li, L. J. High-Quality Thin Graphene Films from Fast Electrochemical Exfoliation. *ACS Nano.* **2011**, *5* (3), 2332–2339.

(33) Tian, S.; He, P.; Chen, L.; Wang, H.; Ding, G.; Xie, X. Electrochemical Fabrication of High Quality Graphene in Mixed Electrolyte for Ultrafast Electrothermal Heater. *Chem. Mater.* **2017**, *29* (15), 6214–6219.

(34) Zhang, Y.; Xu, Y. Simultaneous Electrochemical Dual-Electrode Exfoliation of Graphite toward Scalable Production of High-Quality Graphene. *Adv. Funct. Mater.* **2019**, *1902171*, 1–14.

(35) Chen, C. H.; Yang, S. W.; Chuang, M. C.; Woon, W. Y.; Su, C. Y. Towards the Continuous Production of High Crystallinity Graphene via Electrochemical Exfoliation with Molecular in Situ Encapsulation. *Nanoscale* **2015**, *7* (37), 15362–15373.

(36) Wu, R.; Qu, J.; Chen, Y. Magnetic Powder MnO-Fe2O3 Composite - A Novel Material for the Removal of Azo-Dye from Water. *Water Res.* **2005**, *39* (4), 630–638.

(37) Wang, X.; Zhong, Y.; Zhai, T.; Guo, Y.; Chen, S.; Ma, Y.; Yao, J.; Bando, Y.; Golberg, D. Multishelled Co 3 O 4 -Fe 3 O 4 Hollow Spheres with Even Magnetic Phase Distribution: Synthesis, Magnetic Properties and Their Application in Water Treatment. *J. Mater. Chem.* **2011**, *21* (44), 17680–17687.

(38) Zhao, D.; Liao, X.; Yan, X.; Huling, S. G.; Chai, T.; Tao, H. Effect and Mechanism of Persulfate Activated by Different Methods for PAHs Removal in Soil. *J. Hazard. Mater.* **2013**, *254–255* (1), 228–235.

(39) Davies, M. J.; Gilbert, B. C.; Stell, J. K.; Whitwood, A. C. Nucleophilic Substitution Reactions of Spin Adducts. Implications for the Correct Identification of Reaction Intermediates by EPR/Spin Trapping. *J. Chem. Soc. Perkin Trans. 2* **1992**, No. 3, 333–335.

(40) Wang, Y.; Wang, L.; Yang, T.; Li, X.; Zang, X.; Zhu, M.; Wang, K.; Wu, D.; Zhu, H. Wearable and Highly Sensitive Graphene Strain Sensors for Human Motion Monitoring. *Adv. Funct. Mater.* **2014**, *24* (29), 4666–4670.

(41) Yin, B.; Wen, Y.; Hong, T.; Xie, Z.; Yuan, G.; Ji, Q.; Jia, H. Highly Stretchable, Ultrasensitive, and Wearable Strain Sensors Based on Facilely Prepared Reduced Graphene Oxide Woven Fabrics in an Ethanol Flame. *ACS Appl. Mater. Interfaces.* **2017**, *9* (37), 32054–32064.

(42) Hempel, M.; Nezich, D.; Kong, J.; Hofmann, M. A Novel Class of Strain Gauges Based on Layered Percolative Films of 2D Materials. *Nano Lett.* **2012**, *12* (11), 5714–5718.

(43) Wang, B.; Lee, B. K.; Kwak, M. J.; Lee, D. W. Graphene/Polydimethylsiloxane Nanocomposite Strain Sensor. *Rev. Sci. Instrum.* **2013**, *84* (10).

(44) Bae, S. H.; Lee, Y.; Sharma, B. K.; Lee, H. J.; Kim, J. H.; Ahn, J. H. Graphene-Based Transparent Strain Sensor. *Carbon.* **2013**, *51* (1), 236–242.

(45) Eswaraiah, V.; Jyothirmayee Aravind, S. S.; Balasubramaniam, K.; Ramaprabhu, S. Graphene-Functionalized Carbon Nanotubes for Conducting Polymer Nanocomposites and Their Improved Strain SensingProperties. *Macromol. Chem. Phys.* **2013**, *214* (21), 2439–2444.

(46) Carvalho, A. F.; Fernandes, A. J. S.; Leitão, C.; Deuermeier, J.; Marques, A. C.; Martins, R.; Fortunato, E.; Costa, F. M. Laser-Induced Graphene Strain Sensors Produced by Ultraviolet Irradiation of Polyimide. *Adv. Funct. Mater.* **2018**, *28* (52), 1–8.

(47) Kim, Y. J.; Cha, J. Y.; Ham, H.; Huh, H.; So, D. S.; Kang, I. Preparation of Piezoresistive Nano Smart Hybrid Material Based on Graphene. *Curr. Appl. Phys.* **2011**, *11* (1 SUPPL.), S350–S352.

(48) Boland, C. S.; Khan, U.; Backes, C.; O'Neill, A.; McCauley, J.; Duane, S.; Shanker, R.; Liu, Y.; Jurewicz, I.; Dalton, A. B.; et al. Sensitive, High-Strain, High-Rate Bodily Motion Sensors Based on Graphene-Rubber Composites. *ACS Nano.* **2014**, *8* (9), 8819–8830.

(49) Zhao, J.; He, C.; Yang, R.; Shi, Z.; Cheng, M.; Yang, W.; Xie, G.; Wang, D.; Shi, D.; Zhang, G. Ultra-Sensitive Strain Sensors Based on Piezoresistive Nanographene Films. *Appl. Phys. Lett.* **2012**, *101* (6).

(50) Lee, Y.; Bae, S.; Jang, H.; Jang, S.; Zhu, S. E.; Sim, S. H.; Song, Y. Il; Hong, B. H.; Ahn, J. H. Wafer-Scale Synthesis and Transfer of Graphene Films. *Nano Lett.* **2010**, *10* (2), 490–493.

(51) Liu, Q.; Chen, J.; Li, Y.; Shi, G. High-Performance Strain Sensors with Fish-Scale-Like Graphene-Sensing Layers for Full-Range Detection of Human Motions. *ACS Nano.* **2016**, *10* (8), 7901–7906.

(52) Montazerian, H.; Rashidi, A.; Dalili, A.; Najjaran, H.; Milani, A. S.; Hoorfar, M. Graphene-Coated Spandex Sensors Embedded into Silicone Sheath for Composites Health Monitoring and Wearable Applications. *Small* **2019**, *15* (17), 1–12.

(53) Cheng, Y.; Wang, R.; Sun, J.; Gao, L. A Stretchable and Highly Sensitive Graphene-Based Fiber for Sensing Tensile Strain, Bending, and Torsion. *Adv. Mater.* **2015**, *27* (45), 7365–7371.

(54) Liu, X.; Tang, C.; Du, X.; Xiong, S.; Xi, S.; Liu, Y.; Shen, X.; Zheng, Q.; Wang, Z.; Wu, Y.; et al. A Highly Sensitive Graphene Woven Fabric Strain Sensor for Wearable Wireless Musical Instruments. *Mater. Horizons.* **2017**, *4* (3), 477–486.

(55) Caçado, L. G.; Takai, K.; Enoki, T.; Endo, M.; Kim, Y. A.; Mizusaki, H.; Jorio, A.; Coelho, L. N.; Magalhães-Paniago, R.; Pimenta, M. A. General Equation for the Determination of the Crystallite Size La of Nanographite by Raman Spectroscopy. *Appl. Phys. Lett.* **2006**, *88* (16), 1–4.

(56) Lucchese, M. M.; Stavale, F.; Ferreira, E. H. M.; Vilani, C.; Moutinho, M. V. O.; Capaz, R. B.; Achete, C. A.; Jorio, A. Quantifying Ion-Induced Defects and Raman Relaxation Length in Graphene. *Carbon.* **2010**, *48* (5), 1592–1597.

(57) Zhong, J. H.; Zhang, J.; Jin, X.; Liu, J. Y.; Li, Q.; Li, M. H.; Cai, W.; Wu, D. Y.; Zhan, D.; Ren, B. Quantitative Correlation between Defect Density and Heterogeneous Electron Transfer Rate of Single Layer Graphene. *J. Am. Chem. Soc.* **2014**, *136* (47), 16609–16617.

(58) Mondal, T.; Bhowmick, A. K.; Krishnamoorti, R. Synthesis and Characterization of Bi-Functionalized Graphene and Expanded Graphite Using n-Butyl Lithium and Their Use for Efficient Water Soluble Dye Adsorption. *J. Mater. Chem. A.* **2013**, *1* (28), 8144–8153.